UNIVERSITAT POLITÈCNICA DE CATALUNYA
BARCELONATECH
Escola Superior d'Enginyeries Industrial, Aeroespacial i Audiovisual de Terrassa

Escola Superior d'Enginyeries Industrial, Aeroespacial i Audiovisual de Terrassa - UPC

DEVELOPMENT OF A 1-D SOLVER FOR A SUPERSONIC EJECTOR

Bachelor Thesis
Aerospace Technologies Engineering

Author:
Martínez de Francisco, Alex

Supervisor:
Castilla, Robert

Terrassa, 28th September 2021

Acknowledgments

I would like to start by thanking my thesis tutor, Robert Castilla López, and Llorenç Macià Cid for supporting and advising me throughout the whole process and for always being willing to answers my questions and concerns.

Also I would like to thank to my family, with special affection to my parents, for supporting me always, and for sharing all the bad and good moments of my life.

Finally, I would like to thank, with special affection, to my late cousin Ibón Martínez Cavero, for being my guidance in the most difficult times.

Abstract

The first ejectors were invented in the 1900s, and a lot of research has been done since that time. The fluid mechanics department of the UPC has been searching for an optimal geometry in order to implement it to a supersonic ejector. Researchers Roberto Castilla López and Llorenç Macià have developed a numerical simulator using OpenFOAM[1] in order to analyze the flow inside a supersonic ejector.

They have found that a one dimensional solver (1D model) of the steady flow is needed to interact with the larger and more complex transient solver that is already done. This OpenFOAM CFD solver will allow to find coefficients to adjust the performance of the one dimensional solver. Then, the 1D solver will be used for the optimization process, as it will allow to make a higher number of simulations. The problem with the CFD solver is that, due to its complexity, every simulation takes too much time, making it impossible to carry out an optimization process.

Therefore, the development of a one dimensional solver has been done using Python. The model is capable to compute the performance for a given ejector geometry and to approximate the vacuum level that can be reached.

Honor declaration

I declare that,

the work in this Degree Thesis is completely my own work,

no part of this Degree Thesis is taken from other people's work without giving them credit,

all references have been clearly cited,

I'm authorized to make use of the research group related information I'm providing in this document.

I understand that an infringement of this declaration leaves me subject to the foreseen disciplinary actions by The Universitat Politècnica de Catalunya - BarcelonaTECH.

Thesis: Development of a 1D solver for a supersonic ejector.

Contents

List of Figures

List of Tables

Nomenclature

Symbols

$\dot{m}$	mass flow rate, kg s^{-1}
A	area, m^2
a	sonic velocity, m s^{-1}
d	diameter, m
E_R	error
M	Mach number
P	pressure, bar
Re	Reynolds number
R	gas constant, kJ kg^{-1} K^{-1}
T	temperature, K
V	velocity, m s^{-1}
c_p	specific heat of gas at constant pressure, kJ kg^{-1} K^{-1}
f	friction factor

Greek Symbols

η	isentropic coefficient
γ	isentropic expansion ratio
ν	specific volume, m^3 kg^{-1}
ω	entrainment ratio
ψ	isentropic coefficient of mixing
ρ	density, kg m^{-3}
θ	expansion ratio
ζ	compression ratio

Superscripts

*	critical mode operation of ejector

Subscripts

1	nozzle exit
2	constant area section
3	constant area section after friction losses
c	back pressure
d	diffuser

m	mixed flow
p	primary flow
s	secondary flow
t	nozzle throat
y	location where two stream start to mix

1 Introduction

The supersonic ejector is a device that using the transportation of a fluid is able to give a low-pressure secondary stream the sufficient quantity of energy in order to accelerate it, using only a high-pressure primary jet and without using any mechanical device.

The vacuum ejector-diffuser system is a simple device, with low maintenance and low energy consumption. It is used in numerous industrial applications, such as refrigeration systems, seawater desalination systems, fuel cells, and high altitude test facilities [2].

Other application consist in vacuum generation. The use of ejectors for vacuum generation is present in many different applications. This is because the advantage of time achieved with ejectors, as they are capable to produce vacuum with high velocity. Other applications include object manipulation.

The mechanism consists in using an ejector with a pressure source to achieve vacuum in a secondary chamber. There are ejectors capable of achieving vacuum levels as high as 99%. But, for industrial usage, it is only necessary to obtain vacuum levels of approximately 80%, which is known as 'useful vacuum'.

This project will help previous studies [1] to develop a more efficient ejector device using a one dimensional (1D) model to predict, with sufficient accuracy, the vacuum level that an ejector can reach for a given geometry. The results obtained by the solver will be used to predict more efficient geometries to study with the CFD models.

1.1 Scope of the project

The design of the model will include:

- An schematic of the supersonic ejector used in the project.
- An explanation of the operation carried out by the ejector, as well as the expressions that are involve, along with the study of them.
- Description of the process used to develop the solver.
- Develop of the program to numerically solve the steady flow of the supersonic ejector and the final pressure in vessel.
- Report with the results and conclusions.

The design will not include:

- The development of a new ejector geometry.

1.2 Requirements

The requirements of this project are the following:

- The final report must include an explanation of the basics of compressible flow and the basics of the supersonic ejector.
- The program must be able to solve the steady primary and secondary flow for a given ejector geometry.
- The solver is required to compute a proper approximation of the final pressure in vessel and the percentage of vacuum obtained.
- The numerical implementation must be included and described in the final report.
- It should be verified that the obtained results are acceptable.
- Final results should be included and discussed.

2 State of art

2.1 Historical Background

Since Giovanni Battista Venturi (Bibbiano, Italy, 11 September 1746 – Reggio Emilia, Italy, 10 September 1822) proposed that velocity increments entails pressure decays, mankind has sought for devices capable of work as pumps or compressors without using mobile mechanical components.

Nowadays, there are multiple instruments based on this principle, such as carburetors and paint sprays guns of compressible air. Alongside these components invented in the late 19th century, there is the ejector, as a result of many advances on scientific and engineering camps applied to steam devices.

Particularly for ejectors, their first rudimentary and early applications date back to 1850s [3]. A jet machine may be seen in the "blast pipe", which is located in the smokebox (a volume at the final of the boiler where the smoke and ash are gathered previous going into the chimney) since the first steam locomotives (see Fig. 1). This device was capable of direct exhaust steam of the cylinders through a nozzle, placed at the base of the chimney, achieving a direct reduction of the flue gas pressure and increasing the air flow on the fire. With this machine, the locomotive power was higher than before, and it also provoked the intermittent flow of smoke of the chimney, which is synchronous with the alternate movement of the pistons. This first rudimentary device was called injector. It was the predecessor of the ejector device, although at that time the principles of the injector were not jet fully understood.

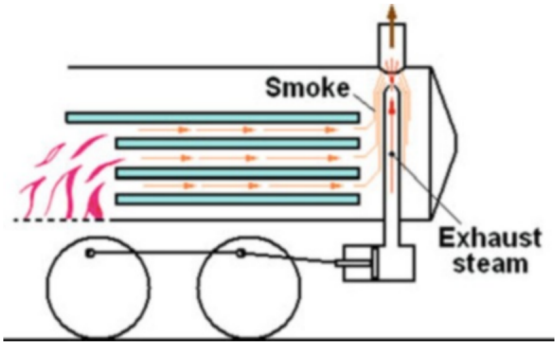

FIGURE 1: Blast pipe in a steam locomotive [3]

Then, the inventor Henri Giffard (locomotive French engineer), who was familiar with the blast pipe, understood the basic principle of the steam injector, and wrote the momentum equation, which is still valid nowadays [4]. After that, he patented the injector in 1858, becoming successful immediately.

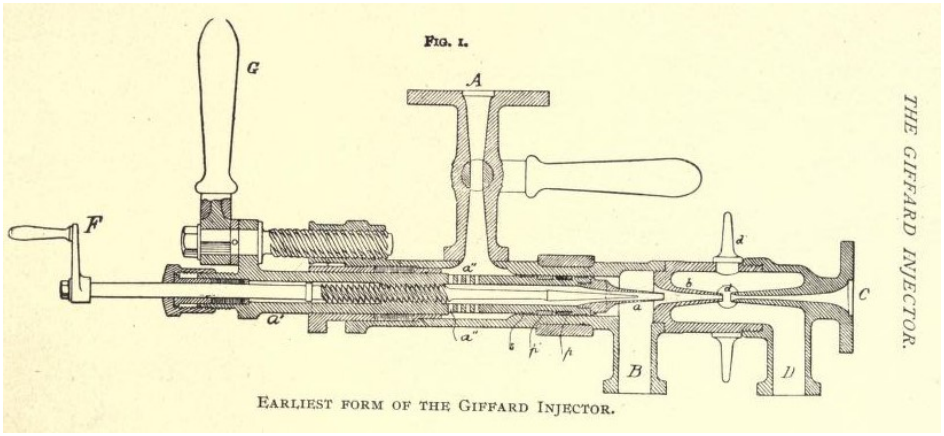

FIGURE 2: First patented injector from Henri Giffard [5]

The injector become very popular by 1860s, as a consequence of its efficiency and simplicity, and ousted the pumps from the locomotives. It was smaller and more efficient, in addition it had not moving parts, which eliminates the necessity of oiling and the majority of friction. In comparison with pumps, injectors were better and also were capable of working during the time the locomotive was not being moving.

Due to all these advantages by 1860 many French railroad and the French Navy lines were using already injectors in their engines, and at the London exhibition of 1862, approximate one third of the steam engines were equipped only with injectors. America started to manufacture injectors in 1860, and just in 1861 nearly 1200 injectors were sold only in the USA. Then at the end of the century (late 1890s - early 1900s), the number of sold injectors increased up to half million, and by that days most of locomotive engineers had never seen one of the elder feed pumps.

In that period, the properties of water vapor were not well-known. The fact that the high enthalpy of the vapor arriving from the boiler is transformed into kinetic energy inside the nozzle and it may overcome a high discharge pressure, once it is transported to the feed water flow, was remarkably hard to comprehend for the engineers of that time. This fact provoked a lively discussion (as mentioned in Kranakis 1982 [4]) and eventually advanced the society in the knowledge and comprehension of the newly born first law of thermodynamics.

Once the working principle of the injector was demonstrated and understood, it was easily transmitted to the steam ejector, and it was used on locomotives as a vacuum pump for the brake circuit (Encyclopædia Britannica 1911 [6], see Fig. 3). For that case, there was a huge availability of steam and combining that with the simplicity ejectors could offer, this system was the perfect solution to the urgent need of a trustworthy braking system (making the vacuum brake system the first technique to be considered safe, in view of the fact that it automatically stops the train, including the case when the circuit is unexpectedly opened to the atmosphere). This vacuum brake system had a major success in the UK, where it was used until the 70s.

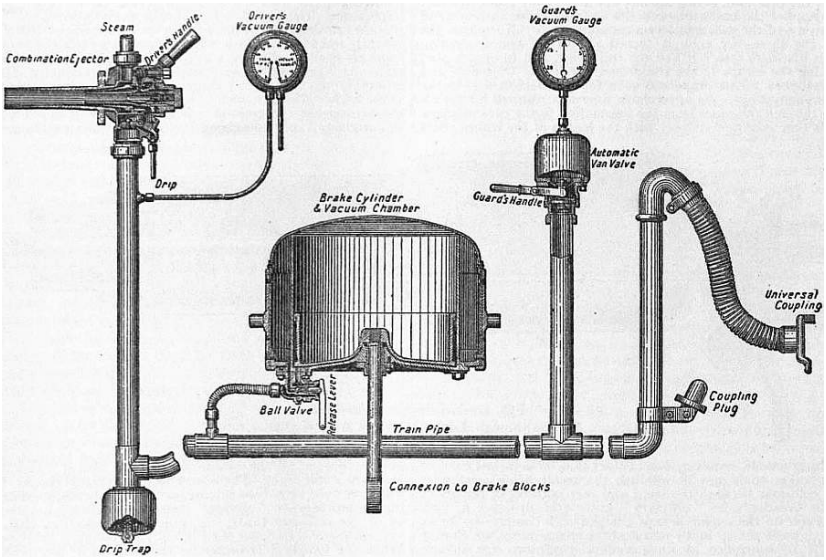

FIGURE 3: Vacuum brake system [6]

Bringing it all together, there was two technical challenges that led to the invention of the ejector. On one side, the needing of devices capable to bring pressurize water into the boiler, which it is the field just discussed. And in the other hand, it was required devices that could extract incondensable gases from the condenser and with the steam available at various pressure levels during the expansion phase, for usage in steam power plants.

This second challenge was addressed by Sir Charles Parson in 1901, who used an steam ejector to solve the challenge, as it was more cheaper and reliable than any other vacuum pump. He gave it the name of "vacuum augmentor". Then, numerous progress were achieved and in 1918 Maurice Leblanc filed the patent "Steam Ejector Aparatus" US Patent 1422582. His idea was to perfect the "vacuum augmentor" developed by Sir Charles Parsons, and its operative system can be observed in Fig. 4. Years later, in the 20s, and taking advantage of the vacuum level the ejector could achieved, it was

proposed as a compressor for refrigeration circuits. Then, this is the predecessor of the ejector as a substitute for the compressor in a refrigeration cycle. Its use began in the 1920s, extending until the 1930s, a period in which it operated with water vapor as refrigerant and heating steam as "motive fluid", being mainly used for the air conditioning of large buildings.

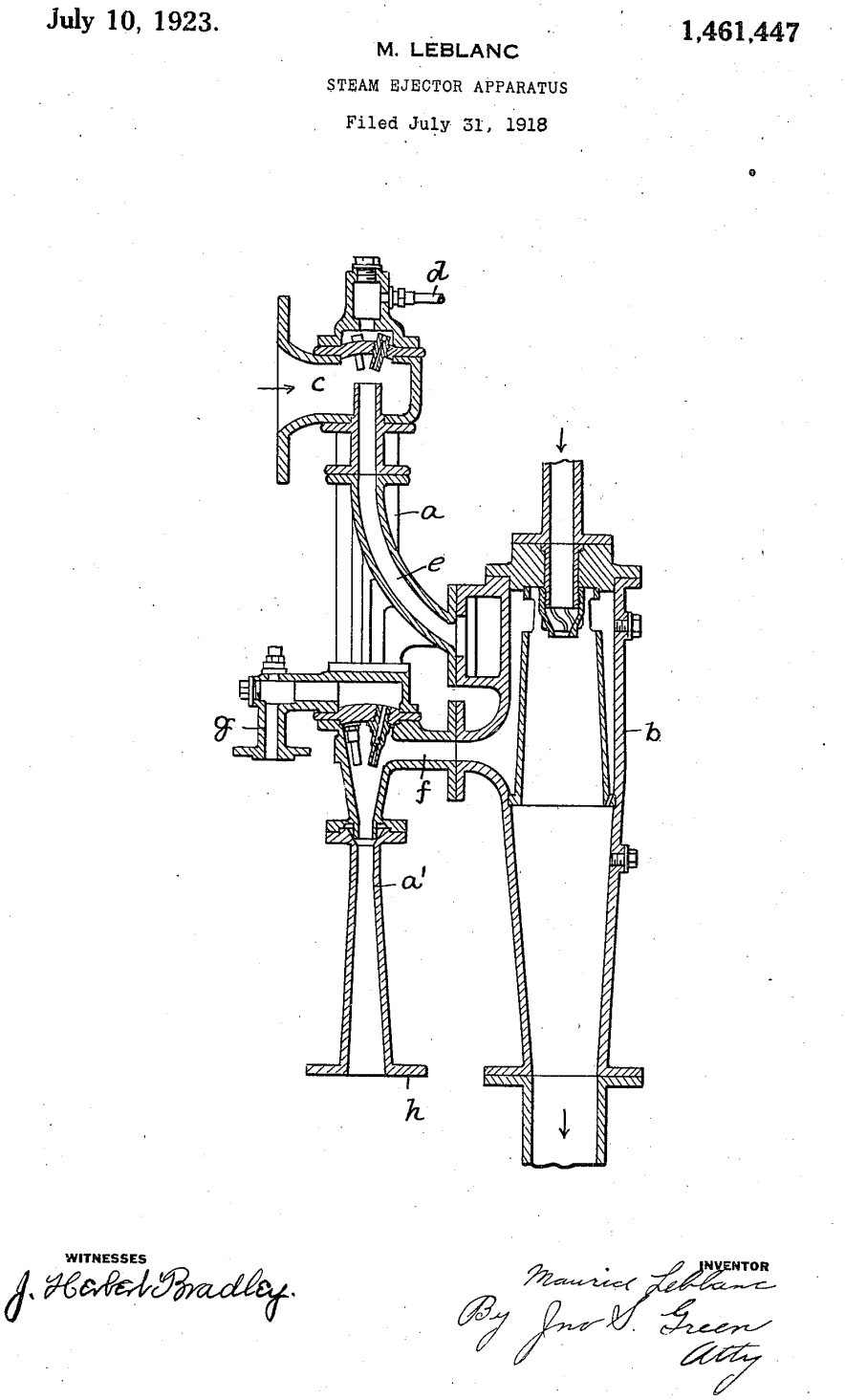

FIGURE 4: First ejector in 1918 [7]

Later it will arrive the introduction of CFCs (chlorofluorocarbon gases) in the 30s, and due to their higher energy efficiency, they practically replaced the ejector from the refrigeration field. Despite this, it has continued to be used in other sectors such as

petrochemical, paper industry (suction pads), steam condensers and other applications where vacuum is required.

From the end of the 80s, and motivated by the energy crises and the growing awareness about the environment (Montreal and Kyoto Protocols), the interest in the improvement of thermodynamic cycles grew, which, although they were already known, they were still far from being able to compete against the compression machine, mainly for reasons of efficiency, cost, and simplicity of operation. The criteria for new designs was to focus on the use of renewable energies and the use of refrigerants that do not affect the environment, which are generally called "natural refrigerants" for their characteristics and origin.

As a consequence, the consolidated working fluids (the CFCs) were replaced in a short time frame, but the refrigeration and air conditioning were still appreciated as a relevant products for the final electricity users. This provoke a renewed interest concerning the heat-powered refrigeration devices and the usage of environmentally secure working fluids. Unfortunately for ejector chillers, the absorption based system were the ones who dominate the market.

Nowadays, even though the absorption system dominate the refrigeration market for the most part, there are investigations in other cycles which are being investigate [8]. Besides the vapor compression cycles, there are alternatives as the thermal energy cycles and electric energy cycles. All of them used for the sake of refrigeration.

One of the thermal energy cycles is based on the ejector, and it is focus on the ejector design and the searching of the ideal refrigerant fluid for the different operational conditions, in order to optimize the process.

2.2 Current situation

Much research has been done in order to determine the performance of ejectors (which can be quantified by its entrainment ratio [9]). The entrainment ratio is the ratio of mass flow between the secondary and primary mass flow rates. There are many theoretical ejector models which are capable of predicting (with margin errors) the performance. These analytical techniques can be classified into two main groups [10]: constant area mixing methods, where the nozzle exit is located inside the constant area, and therefore the mixing of primary and secondary fluids happens inside the constant area section. The other group is the constant pressure mixing methods. It takes place when the nozzle is placed before the mixing chamber, in front of the constant area section. The latter analytic techniques gives superior performances for the ejector above the constant area mixing methods, as shown in [11]. Therefore, the present study will focus in develop a constant pressure mixing model.

The constant pressure of theory ejector developed by Huang et al. [12] was used by many other posterior works and theories [2, 8, 13, 14, 15]. Huang et al. [12] developed a constant mixing model, but with a new feature, consisting in assuming the mixing between two flows inside the constant area section.

In his report [12], Huang et al. shows the theoretical study needed to develop the model. The model consists in the implementation of a one dimensional solver with the R-141b as a working fluid, and then the obtained results are compared with experimental data obtained by his own. The analytical model is capable of predict the ejector performance but only at the critical mode operation (explained later in Subsection 3.2), when the two flows are choked and the ejector is working at fully capacity.

Kong et al. [2] presented an updated 1D evaluation model, which was proposed to predict the ejector performance with reasonable exactitude. The model includes empirical coefficients to take account the losses produce by shock waves and the mixing process, and as a differentiating factor, the model includes the calculation of friction losses solved by momentum and energy conservation equations, alongside with the inclusion of shock wave equations and Fanno flow equations. In this model, the primary flow goes through a convergent nozzle, and the exit is located inside the constant area, which means that this model is based in constant area mixing methods. However, the results show high accuracy when it comes to compute the ejector performance, thanks to the inclusion of a more complex set of equations.

Another theoretical analysis is the one made by Chen et al. [13]. This model is based on constant pressure mixing methods, that are assumed to have a better performance. In addition, this model not only computes the ejector performance for the critic mode operation (as the previous theoretical models do), but also determines the performance for the subcritical mode operation of the ejector. However, it supposes isentropic flows, and it uses isentropic coefficients to take account of the mixing losses.

Javier García del Valle [8], makes a bibliographic review of a high number of existing models in his PhD thesis. He also develops two different mathematical models to predict the ejector performance, and then he compares them with existing models and with his own experimental results. He developed a linearized axisymmetric potential model and a non linearized axisymmetric potential model, with the latter being more complex. This two models resulted to be very accurate compared to the experimental data, but both of them are two dimensional models, and not one dimensional.

3 Methodology

3.1 Working principle of ejectors

A supersonic ejector could take multiple geometries, nevertheless, a basic scheme is presented in Fig. 5. The size and geometry shown are non scaled, but enough to understand how it works. The fundamental parts are the injector, the mixing chamber and the diffuser [16].

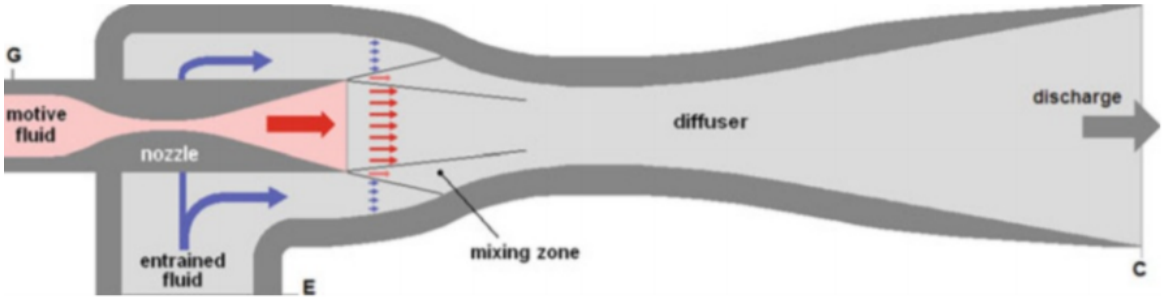

FIGURE 5: Section of a basic standard supersonic ejector [3]

The primary (or motive) flow is supplied through the primary nozzle (called injector). Then, this flow carry along the secondary one (which is also called entrained flow) and pull from it reaching both the mixing chamber, where momentum and energy transfers are done. With highly different velocities, the transfer of momentum cause an acceleration of the entrained flow as long as a deceleration of the motive fluid. Then, once the two flows are mixed into one, the later pass throw the mixing zone up until the diffuser, where eventually is discharge, re-compressing until reaching the ambient pressure.

The ejector works as a substitute of another assembly, much more complex, formed by a turbine and a compressor. The ejector removes the existence of mechanical work transmission trough a connecting shaft, and also have losses from rotating blades, bearings, lubrication, etc.

Nevertheless, the two streams mixing with highly different velocities introduces some energetic losses which should be taken into consideration. There is a transition where the flow goes from supersonic to subsonic, due to the velocity loss. Would be ideal if the transition occurs at the throat of the diffuser, with a progressively decreasing velocity. In that case the flow did not undergo from supersonic flow to subsonic with a shock wave. However, this condition only occurs with a particular inlet and exit conditions,

making it practically impossible to achieve in reality. And as a consequence, normally the supersonic flow decelerates to subsonic through a wave shock.

The stable mode operation of the ejector is reached when the shock takes place downstream of the diffuser next to the throat. This is because, with this condition, flow rates are insensitive to any possible increase in the discharge pressure. While the discharge pressure increases, the shock is moving in the direction of the throat, when eventually it reaches the throat, the ejector experiences its most efficient operation condition (see Fig. 13), as it achieves the maximum entrainment ratio with the maximum discharge pressure.
At this state, any additional increase in the discharge pressure will cause the flow to become subsonic, and then it will become dependent on the discharge pressure. Operating in this condition, the ejector become unstable, and an increments in the discharge pressure causes the performance to step back.

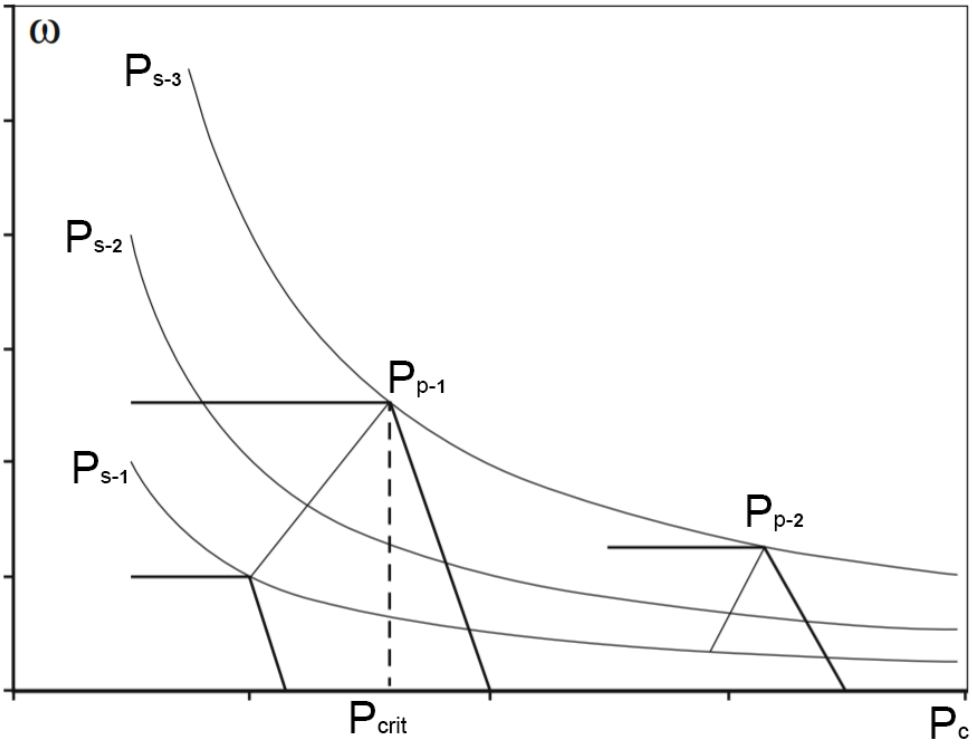

FIGURE 6: Operation map of a supersonic ejector [3]

Fig. 6 shows the above described behavior, in terms of the entrainment ratio. For the sake of clarity, it should be introduced the following non-dimensional parameters:

- Entrainment ratio $\omega = \dot{m}_s/\dot{m}_p$, which is the quotient between the secondary ($\dot{m}_s$) and the primary ($\dot{m}_p$) mass flow rates.

- Compression ratio $\zeta = P_c/P_s$, being the quotient between the discharge (P_c) and induced fluid (P_s) pressures.
- Expansion ratio $\theta = P_p/P_s$, referring to the ratio between the primary (P_p) and entrained fluid (P_s) pressures.

With this parameters, it is possible to discuss the behavior using Fig. 6. At first, for a given primary (P_{p1}) and secondary pressure (P_{s3}) conditions, the entrainment ratio (ω) is a function of the discharge pressure (P_c). The line is first horizontal until it reaches the *critical back pressure* (P_{crit}), also called maximum discharge pressure, and is the limiting operational point, since after reaching it, increasing values in the discharge pressure will lead to decreases of the entrainment ratio. The critical back pressure is the point where the maximum entrainment ratio is reach alongside the maximum compression ratio (ζ_{crit})

Then, if the secondary fluid pressure is lowered (e.g, reach P_{s1} from P_{s3} and at a constant primary pressure), then the operating curve of the ejector is moved left and downward of the chart (referring Fig. 6), which means lower values of both the entrained (ω) and the compression (ζ_{crit}) ratios. Continuing with a primary fluid pressure increase (e.g., primary pressure goes from P_{p1} to P_{p2}), and without changes now in the induced pressure flow (i.e, P_s remains constant at P_{s1}), ζ_{crit} and the expansion ratio (θ) all both increase, and the ω decreases.

Finally, it is worth mentioning that another important parameter is the area ratio between primary nozzle and the mixer/diffuser area sections. This is a limitation factor when the ejector is working in supersonic conditions, as the two flow rates are limited and so is the entrainment ratio. Then, as the area ratio increases, the primary flow increases and the compression ratio increases too. Alongside, the entrainment ratio decreases, as the induced flow remains constant or even decline, as the major section that the primary flow is now occupying at the mixing section.

3.2 Mathematical models

There are many proposed mathematical models in the literature, and the majority have the purpose of obtain the ratio between the secondary ($\dot{m}_s$) and the primary ($\dot{m}_p$) mass flow rates [16]. This indicator is the entrainment ratio:

$$\omega = \frac{\dot{m}_s}{\dot{m}_p} \tag{1}$$

The principal models can be classified into three main groups, which are thermodynamic, energetic and cinematic models, commented in the doctoral thesis of J. García del Valle [8]. The cinematic ones use the whole set of conservation equations: mass, momentum and energy conservation. The model presented in this bachelor thesis is a cinematic model, as it is used the conservation equations to predict the performance of the ejector.

The first cinematic model to describe the different working modes of an ejector is the Fabri and Sienstrunck model [17]. And in addition it is the most instructive model, as it comprehensively describes the three modes of a constant area ejector. The test carried out by [17] were performed by lowering the primary fluid pressure. The three operational modes observed were:

1. **Supersonic mode of operation**

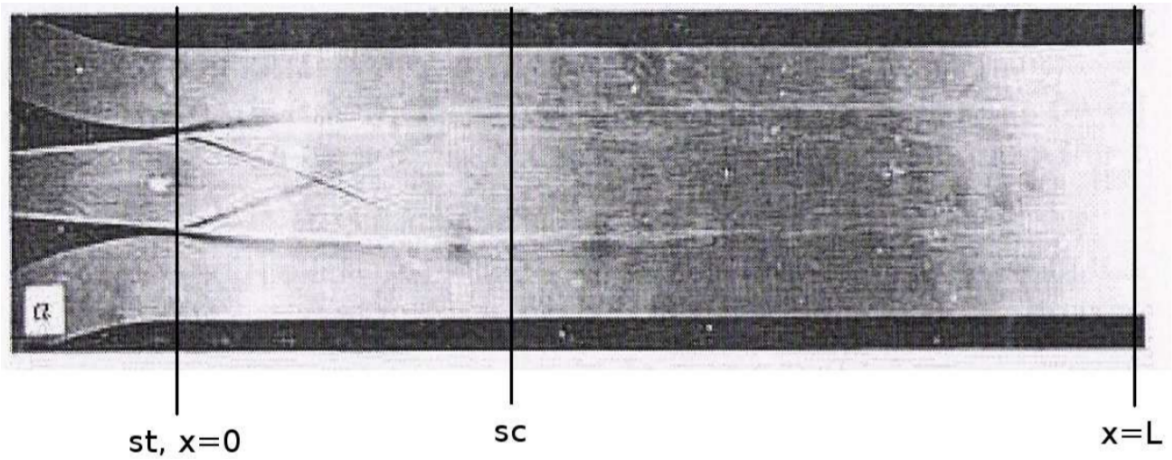

FIGURE 7: Supersonic working operation [17]

This first regime has its own characteristics:

1.1. Stagnation pressure of primary flow is maximum.

1.2. The flow is supersonic at the 'st' section, while the secondary flow is subsonic.

1.3. The critic 'sc' section is unique of this regime, where the secondary flow reaches sonic conditions, as if it was a secondary throat. The primary fluid expands from the 'st' section to the critic 'sc' section.

1.4. The two flows are well distinguished alongside all the tube.

1.5. The pressure at x = L may be different from the discharge pressure, as there is supersonic regime.

2. Saturated supersonic mode

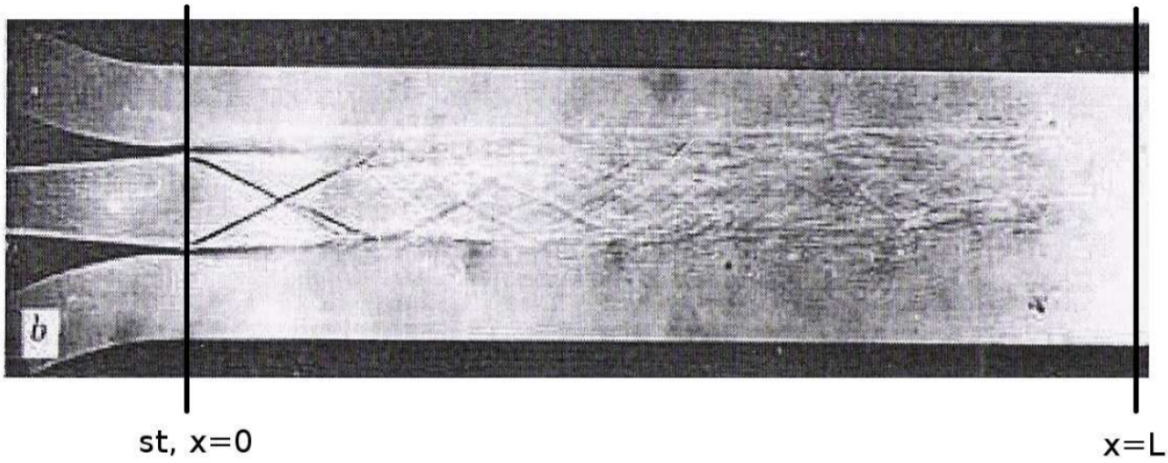

FIGURE 8: Saturated Supersonic working operation [17]

For this second case of operation, the following conclusions are reached:

2.1. The stagnation pressure is less than in the supersonic regime case, with the same stagnation pressure of the secondary pressure and the same discharge pressure.

2.2. For this case, at the 'st' section the primary and the secondary fluids reach supersonic conditions (proved with pressure outlets located at the walls).

2.3. Primary and entrained flows are well distinguished along all the chamber.

2.4. There are no observed shock waves for this operational conditions.

2.5. Discharged pressure may be different from the measured pressure at x = L, this is because the supersonic flow.

3. Mixed mode

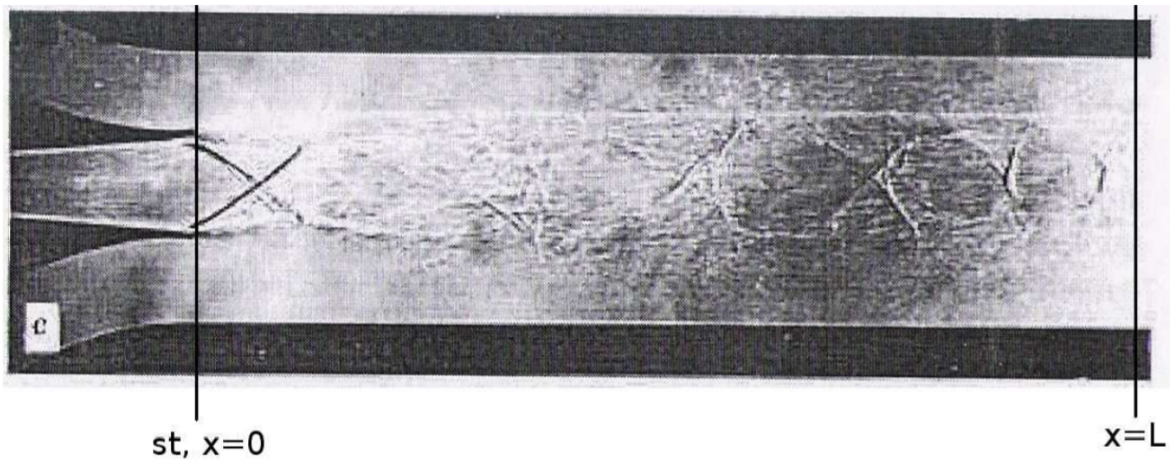

FIGURE 9: Mixed working operation [17]

Observations about this third mode operation:

3.1. Lower needed stagnation pressure for the primary flow than in the supersonic regime case, keeping constant secondary and discharge pressure.

3.2. Primary flow reaches supersonic condition at the 'st' section, while secondary one is subsonic.

3.3. The two flows are mixed between 'st' section and the exit (x = L) section, and oblique chocks are formed as they mix.

3.4. There is subsonic flow at the exit section, which means that the static pressure equals the one existing at the exit, normally the ambient pressure.

The three operational modes observed by Fabri and Sienstrunck [17] are the basis to understand how ejectors work, and then develop theories based on this phenomena. In the following Subsection 3.3, it is explained in detail how these operational modes can be used to determine the performance and how is implemented into the present one dimensional model.

Researches Llorenç Macià and Roberto Castilla have obtained the following results with two different configurations of CFD (more details explained at Section 5). The results only show the secondary flow. Fig. 10 shows the different positions of the generated shock wave. It is seen that for values of $P_s^* \geq 0.4$ the primary flow expands, and the secondary flow reaches sonic conditions between $x = 0$ and $x = L$. This corresponds to supersonic mode of operation.

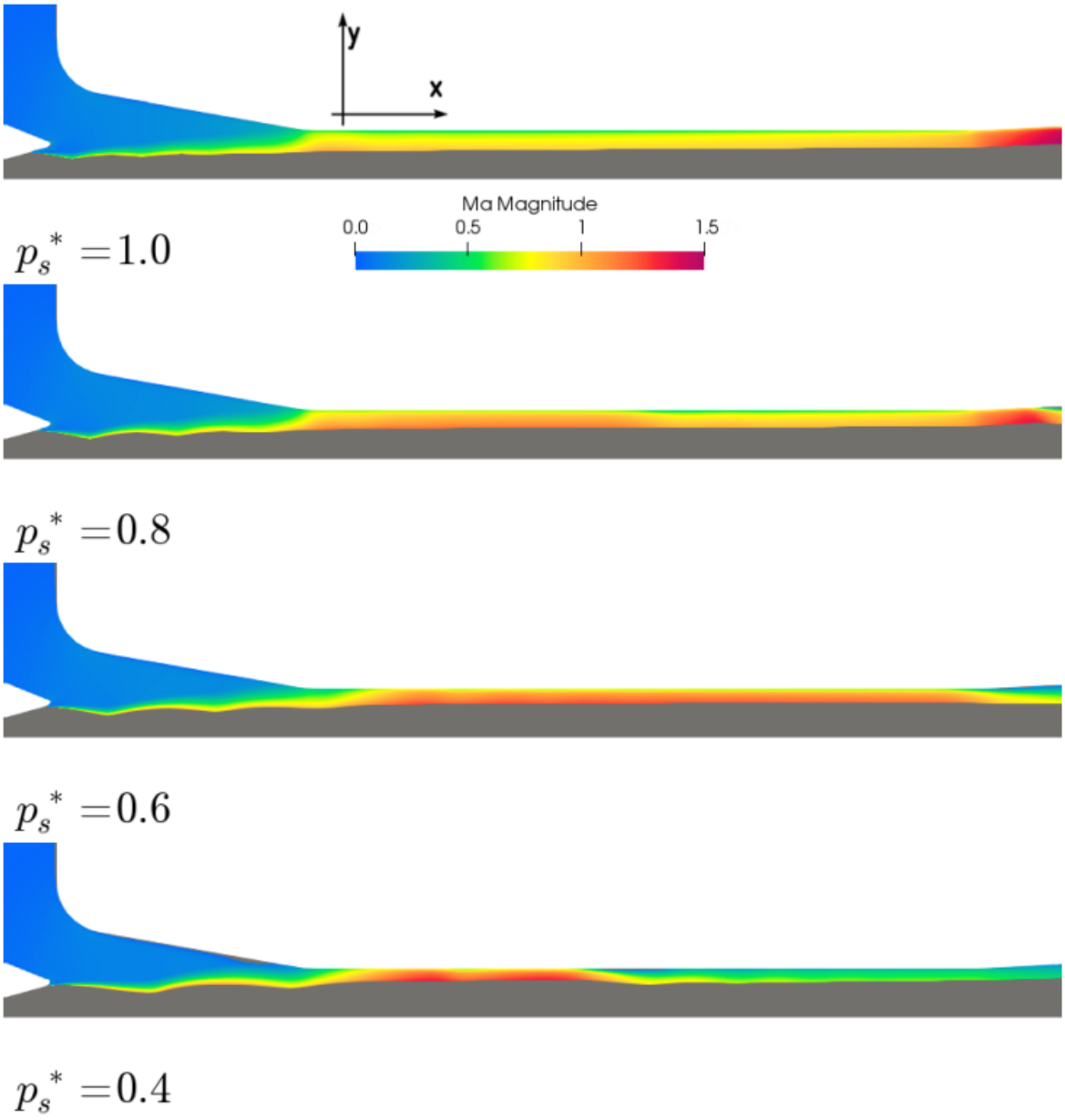

FIGURE 10: Secondary flow with implicit solver HiSA for $P_s^* \geq 0.4$. Flow direction is from the left (inlet) to the right (outlet) [1].

For values of $P_s^* \leq 0.3$, the ejector enters into mixed mode of operation, as the secondary flow does not take a shock wave (the flow does not reach sonic conditions, as any point reaches $M \geq 1$).

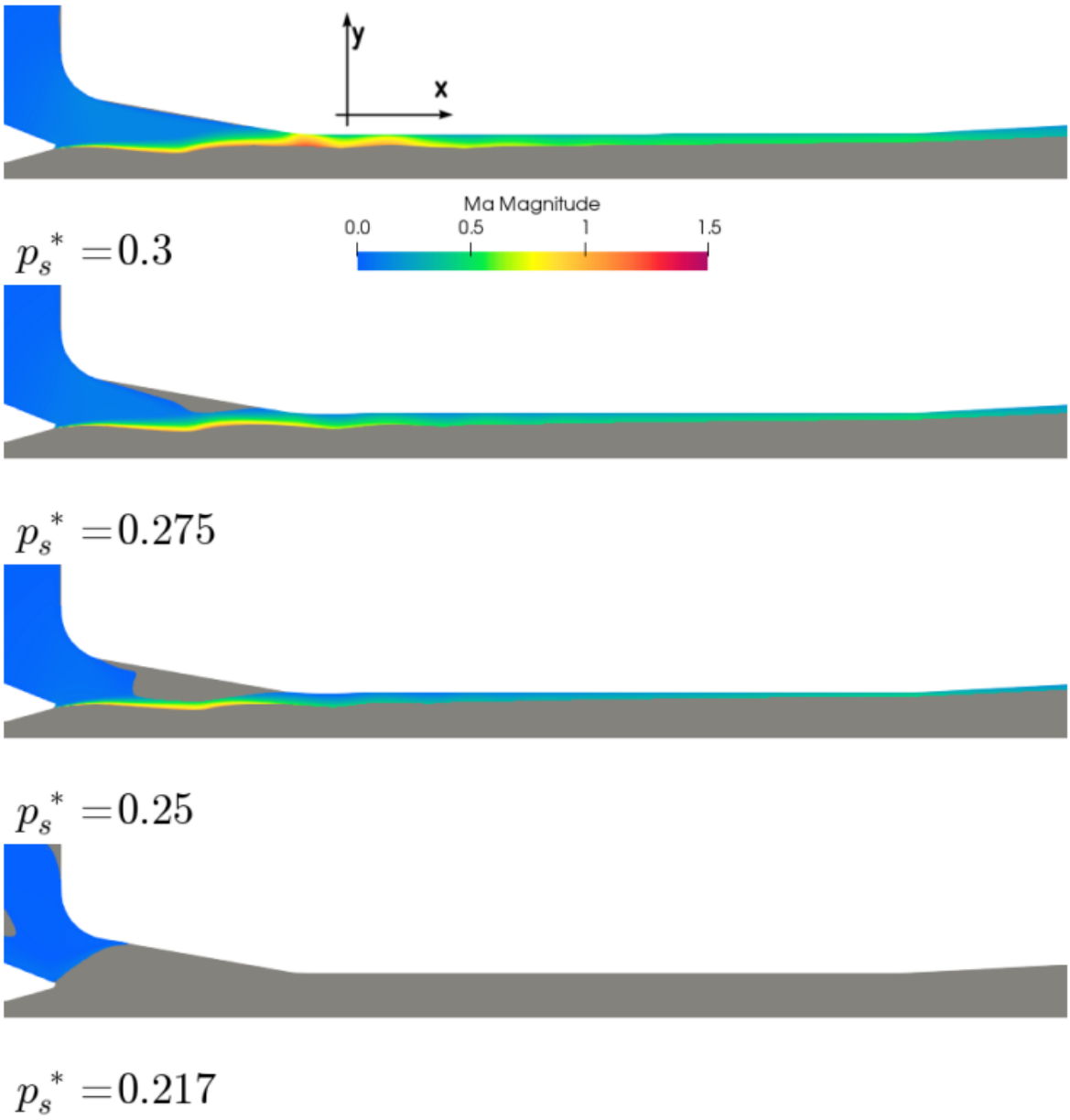

FIGURE 11: Secondary flow for $P_s^* \leq 0.4$ [1].

Finally, Fig. 12 shows the difference between the implicit HiSA and explicit rhoCentralFoam CFD models. For the implicit model, the ejector reaches the maximum vacuum level for $P_s^* = 0.217$ (zero-flow condition for the secondary flow). For the explicit model, the ejector still working at supersonic mode of operation for values of $P_s^* = 0.2$.

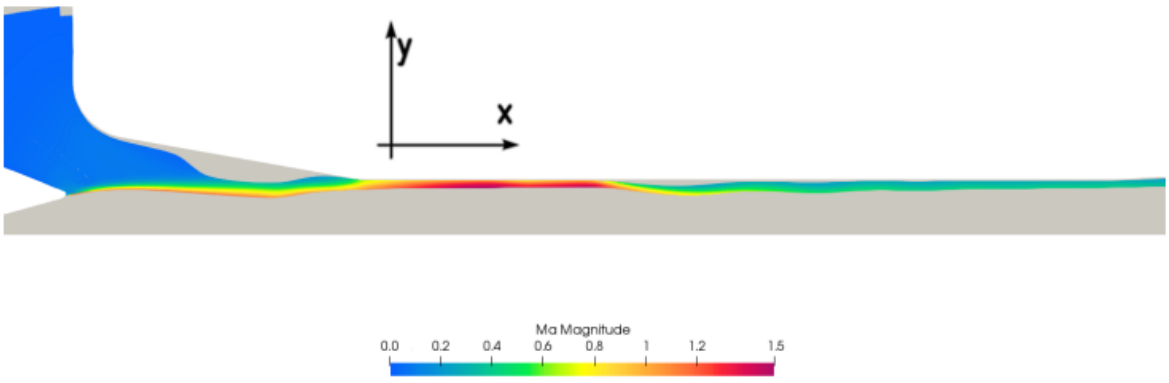

FIGURE 12: Secondary flow with explicit solver rhoCentralFoam for $P_s^* = 0.2$ [1].

3.3 Theoretical analysis of ejector performance

As discussed above, in supersonic ejector applications, the most important indication of ejector performance is the entrainment ratio (ω), shown in Eq. 1.

To evaluate the performance in terms of entrainment ratio, ejector operation can be divided into three modes of operation, as already commented in Subsection 3.2. The Fig. 13 shows the variation of the entrainment ratio in front back pressure when the primary and secondary pressures are constant. During critical mode operation (or double-choking mode), the primary and entrained flows are choked, and then the entrainment ratio reaches its maximum value that stay constant with lower back pressure values. Then, in the sub-critical mode operation (or single-choking mode), it is only the primary flow chocked, and therefore the entrainment ratio changes with the variation of the back pressure. The entrainment ratio goes from its maximum value to zero as the secondary flow decays with higher values of back pressure. For the back flow mode (or breakdown mode), the induced flow could be blocked or reversed, and then the entrainment ratio is zero or less than zero.

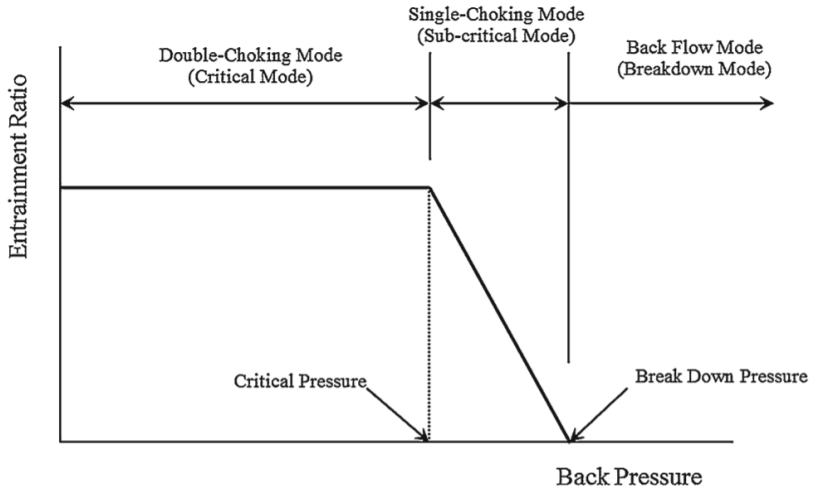

FIGURE 13: Performance of an ejector-diffuser device [2]

Fig. 14 depicts a scheme of an ejector with constant pressure mixing principle. The nozzle exit is located before the mixing chamber. The high pressure stream, typically known as the primary flow, passes through the primary nozzle and fans out at supersonic velocities at the primary nozzle exit (section 1-1). The low pressure environment created by the supersonic primary flow and the viscous entrained effect cause the entrained flow to drawn into the mixing chamber.

The primary flow expands and forms a converging tube for the entrained flow before any mixing with it occurs, following the hypothesis used in [18]. In consequence, the entrained flow accelerates to a sonic velocity inside the constant area section. Then, the mixing process starts when the induced flow is choked for critical mode operation, as suggested by [12].

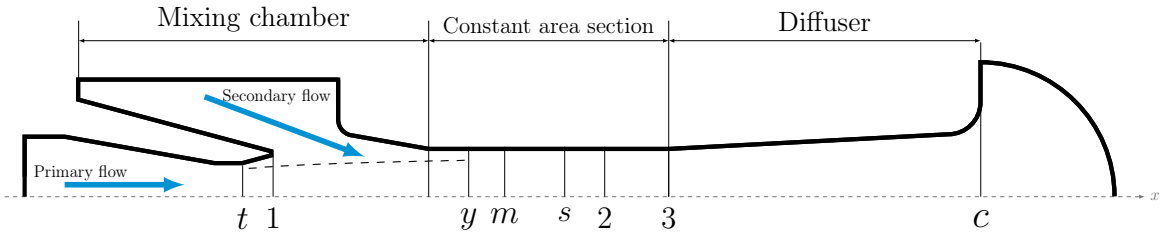

FIGURE 14: Diagram of ejector geometry with sections

For the present model, it is assumed that when the ejector is at critical mode operation, the hypothetical throat occurs inside the constant area section, as suggested by [12]. In addition, when working at subcritical mode operation, it is supposed to exist an effective zone where the entrained flow speed is the highest (but lower than the sonic velocity), and then the two streams are mixed at uniform pressure, as assumed in [13]. This assumption means that there always will be an effective zone (section $y - y$), whether or not the ejector is in critical mode. The mixing process is assumed to start after this section. The mixed fluid undergoes a normal shock wave at the $s - s$ section located within the constant-area section, which causes a significant compression effect and an immediate decrease of the flow velocity. Finally, the mixing flow moves past through the diffuser where the velocity is gradually reduced and the pressure is recovered.

For the analysis of the model, the following assumptions are made:

1. The working fluid is an ideal gas with constant properties c_p and γ
2. The 1D solver is able to compute a one dimensional and steady flow process.
3. The kinetic energy at the primary and secondary flow inlets, and at the exit of the diffuser, is not taking into account, as it can be considered negligible.
4. The accounting of mixing and frictional losses have been taken with the introduction of isentropic efficiency coefficients. Nevertheless, for the implementation of the 1D model, isentropic relations have been used for simplicity.

5. The accounting of frictional wall losses inside the mixing chamber have been considered with the introduction of the Fanno flow equations combined with the Darcy friction factor formulae.

6. The primary flow exits the primary nozzle without mixing with the entrained flow up until the mixing chamber, at the cross section $y - y$. It is then when the two stream begin to mix with uniform pressure, despite the fact that the ejector is in critical or subcritical mode operation.

7. The two streams begin to mix after cross section $y - y$ with uniform pressure (i.e. $P_{py} = P_{sy}$), before the shock wave takes place at section $s - s$.

8. The secondary flow is choked at the hypothetical throat (cross section $y - y$), when the ejector is working in critical mode operation (double-choking mode).

9. The inner wall of the ejector is considered adiabatic.

3.4 Primary flow in the nozzle and suction chamber

3.4.1 Primary flow through nozzle

The primary stream flows into the primary chamber at a given stagnation pressure of P_{p} and a total temperature of T_{p}. The mass flow ($\dot{m}_{\mathrm{p}}$) through the nozzle, at a choking condition, can be obtained using the energy balance law and the isentropic relations:

$$\dot{\mathrm{m}}_{\mathrm{p}} = \frac{\mathrm{P_p A_t}}{\sqrt{\mathrm{T_p}}} \times \sqrt{\frac{\gamma}{\mathrm{R}} \left(\frac{2}{\gamma+1}\right)^{\frac{\gamma+1}{\gamma-1}} \cdot \eta_{\mathrm{p}}} \tag{2}$$

For that case, the coefficient η_{p} is the isentropic efficiency coefficient for the nozzle, which takes into account the friction loss of the compressible flow. The value of the coefficients will be discussed at Subsection 3.5.

Then, it is computed the Mach number at the exit of the nozzle, M_{p1}, and the exit pressure, P_{p1}, using the gas dynamic relations between Mach number, the cross section area of the throat, A_{t} and the exit cross section area A_{p1}. The relations are the following [19]:

$$\left(\frac{\mathrm{A_{p1}}}{\mathrm{A_t}}\right)^2 = \frac{1}{{\mathrm{M_{p1}}}^2}\left[\frac{2}{\gamma+1}\left(1+\frac{\gamma-1}{2}{\mathrm{M_{p1}}}^2\right)\right]^{\frac{\gamma+1}{\gamma-1}} \tag{3}$$

$$\frac{\mathrm{P_p}}{\mathrm{P_{p1}}} = \left(1+\frac{\gamma-1}{2}\mathrm{M_{p1}^2}\right)^{\frac{\gamma}{\gamma-1}} \tag{4}$$

3.4.2 Primary flow core

The entrained flow does not mix with the primary flow while it fans out the nozzle, as they mix at the section $m-m$. Then, the Mach number M_{py} of the primary flow at the $y-y$ section can be obtained using the following isentropic relation:

$$\frac{\mathrm{P_{py}}}{\mathrm{P_{p1}}} = \frac{\left(1+\frac{\gamma-1}{2}\mathrm{M_{p1}^2}\right)^{\frac{\gamma}{\gamma-1}}}{\left(1+\frac{\gamma-1}{2}\mathrm{M_{py}^2}\right)^{\frac{\gamma}{\gamma-1}}} \tag{5}$$

The Mach number M_{py} is computed with the input arguments P_{p1}, P_{py} and M_{p1}. Then it is possible to calculate the area (hypothetical throat) of the primary flow at the $y-y$ section, using the isentropic relation that follows. However, it is included an isentropic

coefficient η_{py} which takes into account the loss of the flow from the $1-1$ section to the $y-y$ section.

$$\frac{A_{py}}{A_{p1}} = \frac{\left(\frac{\eta py}{M_{py}}\right)\left[\frac{2}{\gamma+1}\left(1+\frac{\gamma-1}{2}{M_{py}}^2\right)\right]^{\frac{\gamma+1}{2\cdot(\gamma-1)}}}{\left(\frac{1}{M_{p1}}\right)\left[\frac{2}{\gamma+1}\left(1+\frac{\gamma-1}{2}{M_{p1}}^2\right)\right]^{\frac{\gamma+1}{2\cdot(\gamma-1)}}} \tag{6}$$

Regarding the primary flow up until the section $y-y$, finally it is calculated the temperature of the primary flow at this section.

$$\frac{T_p}{T_{py}} = 1 + \frac{\gamma-1}{2}M_{py}^2 \tag{7}$$

3.4.3 Entrained flow from inlet to section *y-y* (Critical mode)

If the ejector is working in critical mode operation, it is assumed that the induced flow chokes at section $y-y$, and the following equations are valid.

$$M_{sy} = 1, \qquad P_{sy} = P_{sy}^* \tag{8}$$

The P_{sy}^* is the pressure reached by the entrained flow assuming choking condition at $y-y$ section with an hypothetical throat. As assumed critical mode at this Subsection, the actual P_{sy} will be equal to P_{sy}^*.
The pressure of the entrained flow can be obtained from the given inlet stagnant pressure P_s, using the following isentropic relation:

$${P_{sy}}^* = P_s\left(1+\frac{\gamma-1}{2}M_{sy}^2\right)^{\frac{-\gamma}{\gamma-1}} \tag{9}$$

For a given total pressure (P_s) and temperature (T_s), the mass flow rate of the entrained flow ($\dot{m}_s$) is obtained at critical mode operation with the following Eq. (10). Then, the isentropic coefficient η_s is added to account for the losses of the secondary flow:

$$\dot{m}_s = \frac{P_s A_{sy}}{\sqrt{T_s}} \times \sqrt{\frac{\gamma}{R}\left(\frac{2}{\gamma+1}\right)^{\frac{\gamma+1}{\gamma-1}} \cdot \eta_s} \tag{10}$$

3.4.4 Entrained flow from inlet to section *y-y* (Sub-critical mode)

For sub-critical mode operation of the ejector, it is supposed an effective area of the induced flow where its velocity is the highest, but lower than the velocity reached at the critical mode operation. In other words, lower than the speed of sound. Accordingly,

the following relations can be used:

$$M_{sy} < 1, \qquad P_{sy} > P^*_{sy} \tag{11}$$

For this mode of operation, and using conservation of mass and energy, in addition to isentropic relations, the next equations are reached:

$$\frac{T_{sy}}{T_s} = \left(\frac{P_{sy}}{P_s}\right)^{\frac{\gamma-1}{\gamma}} \tag{12}$$

$$P_{sy}\nu_{sy} = RT_{sy}, \tag{13}$$

$$V_{sy} = \sqrt{2\, c_p\, (T_s - T_{sy})}, \tag{14}$$

$$\dot{m}_s = \frac{V_{sy}A_{sy}}{\nu_{sy}}\sqrt{\eta_s} \tag{15}$$

the η_s is the same isentropic coefficient used in Eq. (10). And the area of the secondary flow can be obtained with the following relation:

$$A_{py} + A_{sy} = A_2 \tag{16}$$

where A_{py} is the area used by the primary flow, A_2 is the total area of the cross section $y - y$, and A_{sy} is the searched area of the secondary flow.

3.4.5 Mixed flow at section m-m upstream of the shock

The primary stream is supposed to start the process of mixing with the secondary stream after the cross section y − y, and then a shock takes place with an intense pressure rise at section s − s. Then, it is possible to apply the momentum and energy conservation equation between section y-y and section m-m. The momentum and energy equations are, respectively:

$$\psi_m\,(\dot{m}_p V_{py} + \dot{m}_s V_{sy}) = (\dot{m}_p + \dot{m}_s)\, V_m \tag{17}$$

$$\dot{m}_p\left(c_p T_{py} + \frac{V_{py}^2}{2}\right) + \dot{m}_s\left(c_p T_{sy} + \frac{V_{sy}^2}{2}\right) = (\dot{m}_p + \dot{m}_s)\left(c_p T_m + \frac{V_m^2}{2}\right) \tag{18}$$

Here the V_m is the velocity of the mixed flow and the ψ_m is relevant to the ejector area ratio A_2/A_t and can be calculated using an empirical relation [12]. V_{py} and V_{sy} are

the flow velocities of primary and entrained flows at section $y-y$, which are:

$$V_{py} = M_{py} \cdot a_{py} \qquad a_{py} = \sqrt{\gamma\, RT_{py}} \tag{19}$$

$$V_{sy} = M_{sy} \cdot a_{sy} \qquad a_{sy} = \sqrt{\gamma\, RT_{sy}} \tag{20}$$

And then the Mach number of the mixed flow can be obtained the following equations:

$$M_m = \frac{V_m}{a_m} \tag{21}$$

$$a_m = \sqrt{\gamma\, RT_m} \tag{22}$$

3.4.6 Mixed flow across the shock from section m-m to 2-2

A supersonic shock with a strong pressure increase will occur in the $s-s$ section. Assuming that the mixed flow after the shock undergoes an isentropic process, the mixed flow between section m-m and section $2-2$ within the constant area section has a uniform pressure P_2. Therefore, the following gas dynamic relations exist [20]:

$$\frac{T_2}{T_m} = \frac{\left[2\gamma {M_m}^2 - (\gamma-1)\right]\left[(\gamma-1){M_m}^2 + 2\right]}{(\gamma+1)^2 {M_m}^2} \tag{23}$$

$$\frac{P_2}{P_m} = 1 + \frac{2\gamma}{\gamma+1}\left({M_m}^2 - 1\right) \tag{24}$$

$${M_2}^2 = \frac{1+\frac{\gamma-1}{2}{M_m}^2}{\gamma {M_m}^2 - \frac{\gamma-1}{2}} \tag{25}$$

From the Mach number and the pressure, it is possible to obtain the other flow properties at section $2-2$:

$$\rho_2 = \frac{P_2}{R\, T_2}, \qquad V_2 = M_2\sqrt{\gamma R\, T_2} \tag{26}$$

3.4.7 Wall friction losses at mixing chamber

After the shock wave takes place, the mixed fluid flows across the constant mixing chamber.

To take into account the inner wall friction losses, the calculation of the Darcy friction factor is used, to then use the Fanno flow properties changes [21].

The friction between the flow and the walls of the constant area make the flow properties to change through the duct. The friction inside a tube can be modeled as a shear stress at the wall acting on a fluid with uniform pressures [19], as shown in Fig. 15.

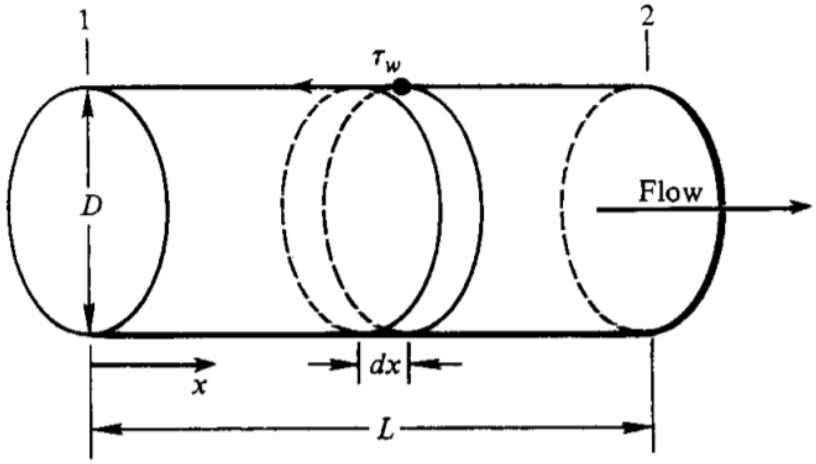

FIGURE 15: One dimensional flow model with friction [19]

Modifying the momentum equation in order to include the frictional shear stress τ_w, that acts on the surface of the inner wall, the momentum equation in his integral form is:

$$\oiint_S (\rho \mathbf{V} \cdot \mathrm{d}\mathbf{S})u = -\oiint_S (\mathrm{p}\mathrm{d}\mathrm{S})_x - \oiint_S \tau_w \mathrm{d}\mathrm{S} \tag{27}$$

If the momentum equation is applied to the boundary conditions of cylindrical control volume of diameter D and length L (as shown in Fig. 15), the Eq. (27) becomes:

$$-\rho_1 u_1^2 \mathrm{A} + \rho_2 u_2^2 \mathrm{A} = p_1 \mathrm{A} - p_2 \mathrm{A} - \int_0^{\mathrm{L}} \pi \mathrm{D} \tau_w \mathrm{d}x \tag{28}$$

For a circular section, the area can be substituted as $A = \frac{\pi D^2}{4}$, and then:

$$(\mathrm{p}_2 - \mathrm{p}_1) + \left(\rho_2 u_2^2 - \rho_1 u_1^2\right) = -\frac{4}{\mathrm{D}} \int_0^{\mathrm{L}} \tau_w \mathrm{d}x \tag{29}$$

The shear stress τ_w varies with distance x along the duct, thus complicating the integration on the right-hand side of Eq. (3.92). This can be circumvented by taking the limit of Eq. (3.92) as L shrinks to dx, as shown in Fig. 3.14, resulting in the differential relation

$$\mathrm{dp} + \mathrm{d}\left(\rho u^2\right) = -\frac{4}{\mathrm{D}}\tau_w \mathrm{d}x \tag{30}$$

Applying the conservative mass equation ($\rho u = \mathrm{cte}$), as the area between two points of the duct remains constant. Therefore, it can be express, $\mathrm{d}\left(\rho u^2\right) = \rho u\ \mathrm{d}u + u\ \mathrm{d}(\rho u) = \rho u \mathrm{d}u + u(0) = \rho u\ \mathrm{d}u$. Thus Eq. (30) becomes:

$$\mathrm{dp} + \rho u \mathrm{d}u = -\frac{4}{\mathrm{D}}\tau_w \mathrm{d}x \tag{31}$$

Finally, the shear stress can be express in terms of a friction coefficient f', which is describes as $\tau_w = \frac{1}{2}\rho u^2 f'$. Substituting this expression to Eq. (31), it becomes:

$$\mathrm{dp} + \rho u\ \mathrm{d}u = -\frac{1}{2}\rho u^2 \frac{4f'\mathrm{d}x}{\mathrm{D}} \tag{32}$$

Returning to Fig. 15, the driving force causing the mean cross-sectional flow properties to vary as a function of x is friction at the wall of the duct, and this variation is governed by Eq. (32). For practical calculations dealing with a calorically perfect gas, Eq. (32) is recast completely in terms of the Mach number M. This can be accomplished by recalling that, $a^2 = \gamma p/\rho, M^2 = u^2/a^2, p = \rho RT, \rho u = \text{const}$, and $c_p T + u^2/2 = \text{const}$. The result is:

$$\frac{4f'\mathrm{d}x}{\mathrm{D}} = \frac{2}{\gamma \mathrm{M}^2}\left(1 - \mathrm{M}^2\right)\left[1 + \frac{\gamma - 1}{2}\mathrm{M}^2\right]^{-1}\frac{\mathrm{dM}}{\mathrm{M}} \tag{33}$$

Integrating Eq. (33) between $x = x_1$ (where $M = M_1$) and $x = x_2$ (where $M = M_2$)

$$\int_{x_1}^{x_2} \frac{4f'\mathrm{d}x}{D} = \left[-\frac{1}{\gamma \mathrm{M}^2} - \frac{\gamma + 1}{2\gamma}\ln\left(\frac{\mathrm{M}^2}{1 + \frac{\gamma - 1}{2}\mathrm{M}^2}\right)\right]_{\mathrm{M}_1}^{\mathrm{M}_2} \tag{34}$$

From the solutions are some physical trends that can be discussed. The effect of the friction on the downstream flow is the next, depending if the flow has a supersonic or subsonic inlet. For supersonic inlet the effect is [19]:

1. Mach number decreases, $\mathrm{M}_2 < \mathrm{M}_1$
2. Pressure increases, $\mathrm{p}_2 > \mathrm{p}_1$
3. Temperature increases, $\mathrm{T}_2 > \mathrm{T}_1$
4. Velocity decreases, $u_2 < u_1$

For subsonic inlet the effect is [19]:

1. Mach number increases, $M_2 > M_1$
2. Pressure decreases, $p_2 < p_1$
3. Temperature decreases, $T_2 < T_1$
4. Velocity increases, $u_2 > u_1$

It is shown that the effect of friction is such that tends the flow towards Mach number M = 1. Fig. 16 shows how the effect of friction tends to accelerate the subsonic flow, and to decelerate the supersonic flow. The point a corresponds to maximum entropy, where the flow is sonic.

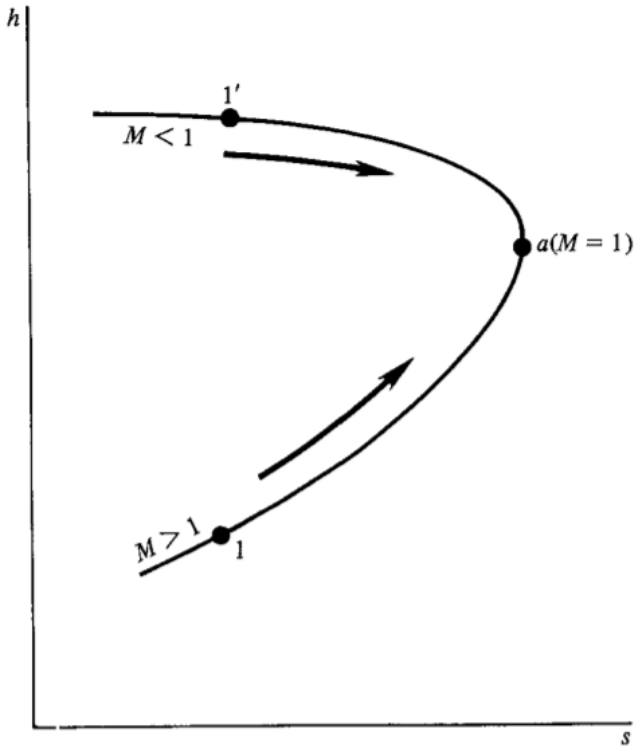

FIGURE 16: The *Fanno curve* [19]

For the calculation of the friction factor f', an alternative one could be used, which is the Darcy-Weisbach friction factor f defined by [22]:

$$f = \frac{\tau}{8\rho u^2} \tag{35}$$

The fanning factor f' is defined by [23]:

$$f' = \frac{\tau}{2\rho u^2} \tag{36}$$

Therefore, the Darcy-Weisbach is four times larger than the fanning friction factor:

$$f = 4 \cdot f' \tag{37}$$

Which can be calculated with the implicit Colebrook-White equation [24]:

$$\frac{1}{\sqrt{f}} = -2.00 \log_{10}\left(2.51\frac{1}{\mathrm{Re}\sqrt{f}} + \frac{1}{3.7}\frac{\varepsilon}{\mathrm{D}}\right) \tag{38}$$

The implicit Colerbook-White equation can not be solver analytically, consequently, it is used an approximation using the Goudar-Sonnad equation for smooth pipe [2]. But first, is needed to compute the Reynolds number:

$$\mathrm{Re} = \frac{\rho_2 \, \mathrm{V}_2 \, \mathrm{d_h}}{\mu} \tag{39}$$

$$\left.\begin{aligned} d &= \tfrac{\ln(10)\mathrm{Re}}{5.02} \\ q &= \ln(d)^{\frac{\ln(d)}{\ln(d)+1}} \\ g &= \ln\left(\tfrac{d}{q}\right) \\ z &= \ln\left(\tfrac{q}{g}\right) \\ \tfrac{1}{\sqrt{f}} &= \tfrac{2}{\ln(10)}\left[\ln\left(\tfrac{d}{q}\right) + z\tfrac{g}{g+1}\left(1 + \tfrac{3z}{6(g+1)^2+2z(2g-1)}\right)\right] \end{aligned}\right\} \tag{40}$$

Once the Darcy friction factor is known, it is possible to integrate Eq. (34) between sections $2-2$ and $3-3$ (where M_1 of the formulae is M_2 and M_2 equals M_3).

To compute for the frictional losses is possible to calculate the resistance coefficient K, where K accounts for the frictional losses $K = f\ L/D$ [25]. Then, the following

equations are used:

$$K = K^*(\mathrm{M}_2) - K^*(\mathrm{M}_3) \tag{41}$$

where $K^*(M)$ is the solution of Eq. (34):

$$K^*(\mathrm{M}) = \frac{1-\mathrm{M}^2}{\gamma \mathrm{M}^2} + \frac{\gamma+1}{2\gamma} \ln\left(\frac{(\gamma+1)\mathrm{M}^2}{2+(\gamma-1)\mathrm{M}^2}\right) \tag{42}$$

Finally, when the mach flow of section $3-3$ is obtained, it is possible to compute the P_3 pressure:

$$\frac{\mathrm{P}_3}{\mathrm{P}_2} = \frac{\mathrm{M}_2}{\mathrm{M}_3}\left[\frac{2+(\gamma-1){\mathrm{M}_2}^2}{2+(\gamma-1){\mathrm{M}_3}^2}\right]^{\frac{1}{2}} \tag{43}$$

3.4.8 Mixed flow through diffuser

Finally the mixed stream passes through the diffuser, and assuming an isentropic process:

$$\frac{\mathrm{P}_c^*}{\mathrm{P}_3} = \left(1 + \frac{\gamma-1}{2} \cdot {\mathrm{M}_3}^2\right)^{\frac{\gamma}{\gamma-1}} \tag{44}$$

3.5 Procedure

The performance of an ejector is defined by the total pressure and temperature at the inlet of the primary nozzle (P_p, T_p), and the total pressure and temperature (P_s, T_s) at the inlet of the suction chamber. Then, to determine the performance, it is also necessary to know the geometrical characteristics, as the nozzle throat diameter d_t (or nozzle throat area A_t), the nozzle exit diameter d_1 (or nozzle exit area A_1) and constant area section diameter d_2 (or constant area section area A_2). The longitude of the constant section area L is necessary also to determine the pressure losses for friction inside it.

The numerical procedure follows the diagram shown in Fig. 17. The value calculation of P_c^* is a crucial step, and then the reference value of the back pressure P_c is given (when is running the ejector in a test bench, the reference P_c will be the ambient pressure outside). If P_c is less than P_c^*, the ejector is working at critical operation. Otherwise, the subcritical operation is running (as shown in Fig. 13).

The results of the analysis with the 1D model include the primary mass flow rate $\dot{m}_p$, the secondary mass flow rate $\dot{m}_s$ and the entrainment ratio ω. In the present model, the default coefficients are taken from [1]. The coefficients should be taken accordingly with the ejector is being studied.

For the present thesis, the ejector coefficients, as the geometry characteristics are not shown, as the results are based on a research ejector studied in the Polytechnic Catalonia University.

Regardless, to bring to the knowledge of the reader, other coefficients used by other authors [12] are the following. Coefficients that take into account the losses in the primary flow nozzle and from the nozzle outlet to section y − y are taken as $\eta_p = 0.95$ and $\eta_{py} = 0.88$, and the coefficient of losses in the entrained flow is taken as $\eta_s = 0.85$, this are the experimental coefficients found by [12] for their studied ejector. It was also found that the coefficient, ψ_m, presented in Eq. (17) is more sensitive than the other coefficients, and therefore it should be taken accordingly to the area ratio, A_2/A_t, and then an empirical relationship was found [12]:

$$\psi_m = \begin{cases} 0.80, & \text{for } A_2/A_t > 8.3 \\ 0.82, & \text{for } 6.9 \leq A_2/A_t \leq 8.3 \\ 0.84, & \text{for } A_2/A_t < 6.9 \end{cases} \tag{45}$$

As mentioned above, equations are similar to the model proposed by [12] and [13] because of the same classical 1D theory, which is based on the conservation of mass, momentum and energy. However, the present 1D model shows different procedure than [12] at the critical mode, and added the subcritical mode of operation.

In the model of Huang et al., the critical pressure $P_c{}^*$ is an independent parameter (obtained from experimental results). Then there is an iteration process with the aim of obtain a theoretical critical pressure which equals the experimental P_c^* by changing the area of the constant area section (A_2). For this reason, the entrainment ratio is obtained using the theoretical A_2 gotten from the model (and not the experimental A_2 result).

In the present model the critical pressure P_c^* is not an independent parameter (as P_c is a required parameter which compares to P_c^*), and also the entrainment ratio w (computed with the experimental value of A_2) and P_c^* are output variables. Similar to [13], the model computes the performance from a given geometry, but for the present model are added Fanno flow equations combined with the Darcy factor formulae to take into account frictional losses.

TABLE 1: Conventional calculation procedure

Step	Inputs	Equations	Outputs	Comments
1	P_p, T_p, A_t	$m_{\mathrm{p}} = \frac{P_{\mathrm{p}} A_{\mathrm{t}}}{\sqrt{T_{\mathrm{p}}}} \times \sqrt{\frac{\gamma}{\mathrm{R}} \left(\frac{2}{\gamma+1}\right)^{(\gamma+1)/(\gamma-1)}} \sqrt{\eta_{\mathrm{p}}}$	m_{p}	Using A_t choking condition, it is possible to compute the mass flow rate through a gas dynamic relation.
2	A_{p1}	$\left(\frac{A_{p1}}{A_t}\right)^2 = \frac{1}{M_{\mathrm{p1}}^2} \left[\frac{2}{\gamma+1}\left(1 + \frac{\gamma-1}{2} M_{\mathrm{p1}}^2\right)\right]^{(\gamma+1)/(\gamma-1)}$	M_{p1}	Using an approximate method calculation, it is possible to compute the Mach no. M_{p1}.
3	M_{p1}	$\frac{\mathrm{P_p}}{\mathrm{P_{p1}}} = \left(1 + \frac{\gamma-1}{2} \mathrm{M_{p1}^2}\right)^{\gamma/(\gamma-1)}$	$\mathrm{P_{p1}}$	Once M_{p1} is known, the next step is calculate the dynamic pressure of the primary flow.
4	P_s	$P_{\mathrm{sy}}^* = P_{\mathrm{s}} \left(1 + \frac{\gamma-1}{2} \mathrm{M_{sy}^2}\right)^{-\gamma/(\gamma-1)}$	P_{sy}^*	It is time to estimate the secondary flow pressure, and it is taken first the pressure assuming sonic conditions.
5	$P_{py} = P_{sy}$	$\frac{\mathrm{P_{py}}}{\mathrm{P_{p1}}} = \frac{\left(1+((\gamma-1)/2)\mathrm{M_{p1}^2}\right)^{\gamma/(\gamma-1)}}{\left(1+((\gamma-1)/2)\mathrm{M_{py}^2}\right)^{\gamma/(\gamma-1)}}$	M_{py}	Using the obtained secondary flow pressure at section $y-y$, the Mach number of the flow is computed.
6	M_{py}	$\frac{\mathrm{A_{py}}}{\mathrm{A_{p1}}} = \frac{\left(\frac{\eta py}{M_{py}}\right)\left[\frac{2}{\gamma+1}\left(1+\frac{\gamma-1}{2}M_{py}^2\right)\right]^{\frac{\gamma+1}{2(\gamma-1)}}}{\left(\frac{1}{M_{p1}}\right)\left[\frac{2}{\gamma+1}\left(1+\frac{\gamma-1}{2}M_{p1}^2\right)\right]^{\frac{\gamma+1}{2(\gamma-1)}}}$	A_{py}	The η_{py} isentropic coefficient represents the flow losses from the $1-1$ to the $y-y$ section.
7	A_{py}	$\mathrm{A_{sy}} = \mathrm{A_2} - \mathrm{A_{py}}$	$\mathrm{A_{sy}}$	This step is necessary to compute the effective area for the secondary flow.
8	P_s	$m_{\mathrm{s}} = \frac{P_{\mathrm{s}} A_{\mathrm{sy}}}{\sqrt{T_{\mathrm{s}}}} \times \sqrt{\frac{\gamma}{\mathrm{R}} \left(\frac{2}{\gamma+1}\right)^{(\gamma+1)/(\gamma-1)}} \sqrt{\eta_{\mathrm{s}}}$	m_s	Secondary mass flow accounting of the isentropic efficiency (η_s)
9	T_s	$\frac{\mathrm{T_{sy}}}{\mathrm{T_s}} = \left(\frac{\mathrm{P_{sy}}}{P_{\mathrm{s}}}\right)^{(\gamma-1)/\gamma}$ $\mathrm{P_{sy}} \nu_{\mathrm{sy}} = \mathrm{RT_{sy}}$ $\mathrm{V_{sy}} = \sqrt{2\mathrm{C_p}\left(\mathrm{T_s} - \mathrm{T_{sy}}\right)}$	$T_{sy}, \nu_{\mathrm{sy}}, V_{sy}$	With the initial secondary flow temperature, it is computed the temperature, specific volume and velocity.
10	T_p, M_{py}	$\frac{\mathrm{T_p}}{\mathrm{T_{py}}} = 1 \pm \frac{\gamma-1}{2} \mathrm{M_{py}^2}$	T_{py}	The temperature of the primary flow is evaluated
11	T_{py}	$V_{py} = M_{py} \cdot \sqrt{\gamma R T_{py}}$	V_{py}	Next step is to compute the velocity of the primary flow, using the previous temperature and the Mach obtained at step 5.
12	V_{py}, V_{sy}	$\psi_{\mathrm{m}} \left(m_{\mathrm{p}} \mathrm{V_{py}} + m_{\mathrm{s}} \mathrm{V_{sy}}\right) = \left(m_{\mathrm{p}} + m_{\mathrm{s}}\right) \mathrm{V_m}$	V_m	ψ_{m} used as a mixed flow coefficient, taking account of the losses.
13	V_m	$m_{\mathrm{p}} \left(\mathrm{C_p T_{py}} + \frac{\mathrm{V_{py}^2}}{2}\right) + m_{\mathrm{s}} \left(\mathrm{C_p T_{sy}} + \frac{\mathrm{V_{sy}^2}}{2}\right) = \left(m_{\mathrm{p}} + m_{\mathrm{s}}\right) \left(\mathrm{C_p T_m} + \frac{\mathrm{V_m^2}}{2}\right)$	T_m	Use of the obtained temperatures, velocities and mass flow rate of each flow to obtained the mixed flow velocity.

TABLE 1: Continuation

Step	Inputs	Equations	Outputs	Comments
14	T_m	$M_m = \frac{V_m}{\sqrt{\gamma R T_m}}$	M_m	The temperature obtained in the previous step is used to compute the Mach number.
15	$P_m = P_{sy}$	$\frac{P_2}{P_m} = 1 + \frac{2\gamma}{\gamma+1}\left(M_m^2 - 1\right)$	P_2	The flow is resolved after the shock wave.
16	M_m	$M_2^2 = \frac{1+\frac{\gamma-1}{2}M_m^2}{\gamma M_m^2 - \frac{\gamma-1}{2}}$	M_2	Mach number of the flow after the shock wave is computed.
17	Re	$\frac{1}{\sqrt{f}} = -2.00\log_{10}\left(2.51\frac{1}{Re\sqrt{f}} + \frac{1}{3.7}\frac{\varepsilon}{D}\right)$	f	Calculation of the Darcy-Weisbach friction factor
18	f, L, D, M_2	$K = K^*(M_2) - K^*(M_3)$	M_3	Computing the Mach flow after the constant section area
19	P_3, M_3	$\frac{P_{c^*}}{P_3} = \left(1 + \frac{\gamma-1}{2}M_3^2\right)^{\gamma/(\gamma-1)}$	P_c^*	Finally, flow pressure at the diffuser exit is calculated.

Table 1 shows the detailed procedure used for the present one dimensional model. The procedure corresponds to the computation of the critical mode operation. The final step is to compute P_c^* and compare it to P_c:

$$\text{If} \quad P_c^* \geqslant P_c \longrightarrow \text{Working at critical mode} \tag{46}$$

$$\text{If} \quad P_c^* \leqslant P_c \longrightarrow \text{Working at sub-critical mode} \tag{47}$$

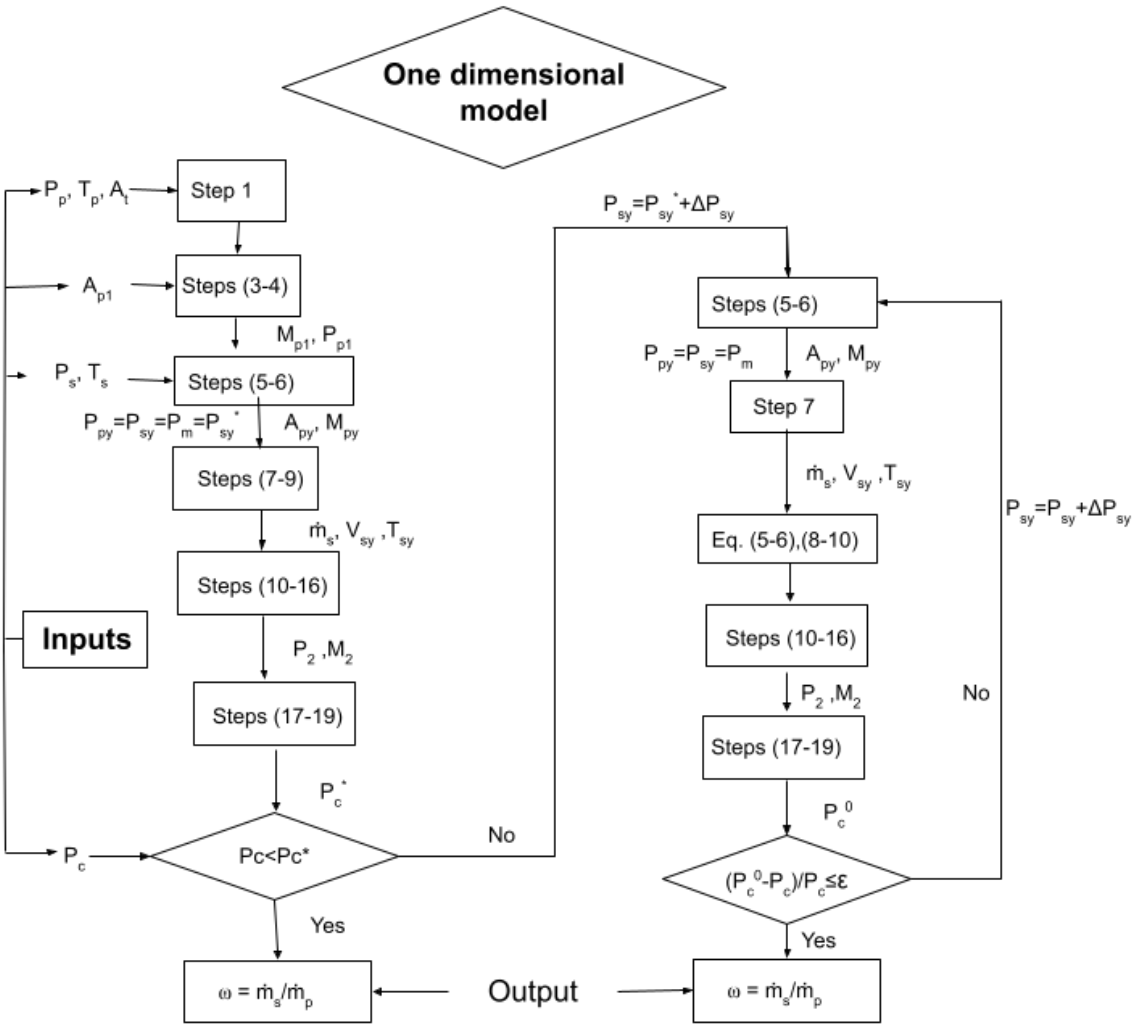

FIGURE 17: Calculation flowchart of the model

4 Model validation

The proposed model computes primary and entrained mass flow rates for different pressures of the secondary flow, and determines the lowest value of pressure that the ejector is capable of reach for a given geometry. In order to measure its accuracy, data from different experimental studies is obtained and used to compare the results.

First, to verify the present model at critical mode operation, experimental data from Hemidi et al. [15] is used. In order to adapt the present model to the geometry characteristics used for Hemidi et al., the same geometry is taken. The characteristics of the air ejector are $d_t = 3.3\,\text{mm}$, $d_1 = 4.5\,\text{mm}$ and $d_2 = 7.6\,\text{mm}$. Then, different stagnation pressures of the primary fluid are used, in order to compare the different results of the model with the experimental data. The following table (see Table 2) shows the error ($E_R = \frac{\text{theory}-\text{experiment}}{\text{experiment}}$) between different measures of different flows (different P_p). The induced pressure is set to be the same as the one used for the experiments ($P_s = 10^5\,\text{Pa} = 1\,\text{bar}$).

TABLE 2: Data comparison to Hemidi et al. [15]

P_p	Experimental ω_{exp}	Present model ω	Error (E_R)
$4 \times 10^5\,\text{Pa}$	0.76	0.88	15.79 %
$5 \times 10^5\,\text{Pa}$	0.62	0.67	8.06 %
$6 \times 10^5\,\text{Pa}$	0.51	0.53	3.92 %

The analysis shows that the theoretical results bring by the present 1D model coincide reasonably with the experimental ones, as the largest error is no more than 16%, and with closer results as the primary pressure increases, being the error with a primary pressure of $P_p = 6 \times 10^5\,\text{Pa}$ between the present model and the experimental data less than 4%.

Then, data collected from previous study made by Llorenç Macia et al. (2019)[1] is utilized. The present model is adapted to the geometrical conditions of [1], in order to have the same conditions, and also the inlet/outlet conditions are set to be the same. The geometry conditions are not shown, but the ejector has circular cross-sections, with different diameters for the primary and exit nozzles, and with other diameter for the mixing tube.

Operation conditions of the 1D model are set to be the same as the experiment, which are stagnation pressure for the primary flow of $P_p = 7 \times 10^5\,\text{Pa}$ and temperature of

$T_p = 20°$ and initial stagnation pressure for the entrained flow of $P_s = 1 \times 10^5$ Pa and temperature of $T_s = 20°$. The properties such as c_p or γ are given in consideration of the working fluid, which is air. Then, the secondary pressure is decreased from the initial value until the entrainment flow becomes blocked, point where the ejector can not decrease more the entrained pressure, and therefore the maximum vacuum level is reached.

Fig. 18 shows the error (E_R) between the entrainment ratio (ω) of the experimental data and the theoretic values of the present model. It is seen that as closer the entrainment ratio gets to zero, the values become more inaccurate, and the differences between the results of the 1D solver and experimental could be very high. For example, in the model the entrainment flow is blocked for values of less than $P_s = 0.20$ bar and experimental data shows that the entrainment flow is blocked for $P_s = 0.19$ bar. Then, the error between these two points become 100%. However, is the relative error which can be very high, regardless the total error between the experimental data and the values shown by the present model, that remains constant.

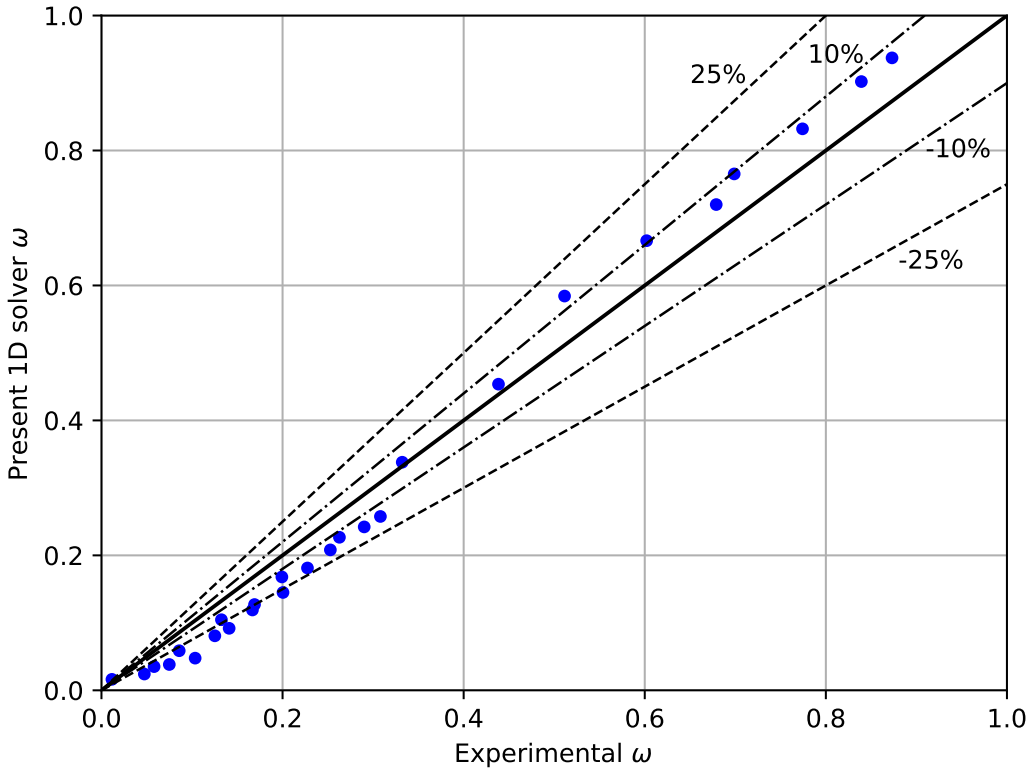

FIGURE 18: Entrainment ratio comparison between present model and experimental data

As shown in Fig. 18, the 1D model becomes more accurate with higher values of ω. The maximum displayed error is about 25% (for data above $\omega_{exp} > 0.15$), but most data point are within $\pm 10\%$. The deviations are generally because of the calculation error from the empirical equations as consequence of the assumptions and the inaccuracy with the isentropic coefficients.
Even though, the present 1D model is capable to resolve the ejector performance with high fidelity, and it can be used to compute the maximum vacuum level of an ejector with a given geometry.

5 Results

The present model is made to achieve the blocked condition and the vacuum level of an ejector with a given geometry. In order to display the results that the model is capable to reach, the geometry of [1] is taken. Fig. 22 shows the results of the entrainment ratio (ω) for different values of the inlet pressure, where P_s^* is the normalized inlet pressure: $P_s^* = P_s/bar$. Then, the results are represented with the experimental data in the same figure, to compare them. The error in the experimental results is also included.

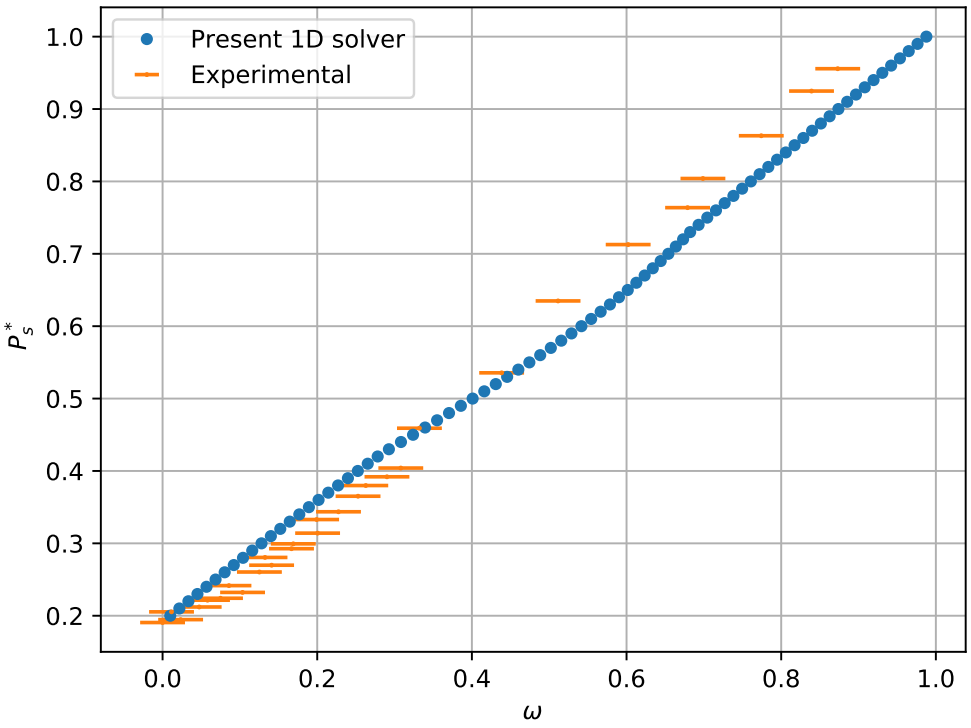

FIGURE 19: Comparison to experimental data

It is seen reasonably accurate data, with values of secondary mass flow relatively closed to the experimental ones. However, differences between higher values seems to be mainly constant, as the differences between lower values of mass flow tend to be slightly diverse, while the model brings a vacuum level of 80% as the experiment brings 81%. This could happen because of the nature of the model. The model is set to have one shock wave between the section $y - y$ and $3 - 3$. But in reality the shock wave is displaced towards the throat, as the secondary pressure decreases. It is difficult to determine where the shock wave takes place in a one dimensional model, and the best that can be done is to assume a shock wave where it normally takes place, and this is the mixing section.

It is not in the scope of this work to make a CFD solver, but Macia et al. [1] used in their study two different density-based solvers, with the purpose of comparison. One of them is the HiSA implicit solver. It is an open source transient solver capable of solving unsteady flows and it works very well with high Mach numbers. The other model is an explicit solver, which is available in the standard distribution of OpenFOAM, rhoCentralFoam (RCF), and it is a transient density-based solver. Results of both solvers are utilized to compare with the present 1D model. Fig. 20 and Fig. 21 show the entrainment ratio in front of the secondary pressure, and the results of the three solvers are compared.

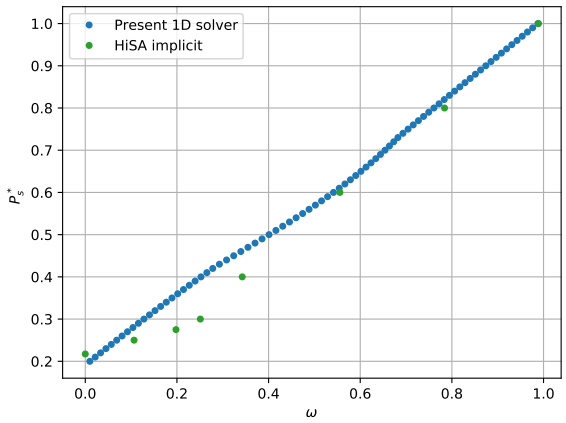

FIGURE 20: Comparison to HISA solver

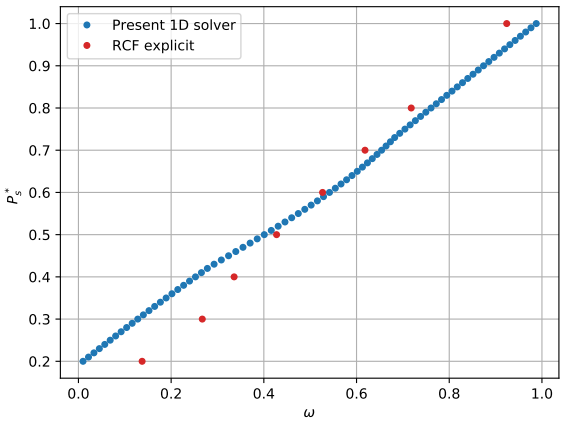

FIGURE 21: Comparison to RCF

The present model shows high accuracy with the implicit HiSA solver (Fig. 20), but it differs more with the RCF explicit solver (Fig. 21). The entrainment ratio computed by the HiSA and the present 1D model are almost the same for high values of P_c, but then the one dimensional model brings more linear results in comparison with the CFD. This could be happening as consequence of placing the shock wave after the mixing process. The HiSA model is able to determine where the shock wave is placed and then it can be more precise. However, the vacuum level calculated by both solvers are considerably the same, as the HiSA model yields a minimum $P_c = 21.730\,\text{kPa}$, which represents a vacuum level of 78.27%, in front of the 80% of the present model.
In other hand, the RCF explicit solver seems to have similar results for high pressure inlet values ($P_s^* > 0.5$). Then, the differences in the results increase. Table 3 shows the entrainment ratio for different values of the inlet pressure.

TABLE 3: Data comparison with RCF explicit solver [1]

P_s^*	RCF solver ω	Present model ω	Error (E_R)
0.4	0.3359	0.2525	24.8 %
0.3	0.2672	0.1280	52.1 %
0.2	0.1374	0.0099	92.8 %

The RCF explicit solver tends to overestimate the values of flow rate and entrainment ratio for low values of P_s^*, as commented in [1] (in Fig. 22 this fact can be observed). For a secondary pressure of $P_s^* = 0.2$, the present 1D model obtained $\omega = 0.0099$ for the entrained ratio, while the experimental results reveal $\omega = 0.0116 \pm 0.029$, which is a very low entrainment ratio. However, the RCF reports an entrainment ratio of $\omega = 0.1374$, which is almost ten times more than the one get by experimental results.

Fig. 22 shows the results of the present model all in one figure with the experimental results, and the HiSA, and RCF solvers.

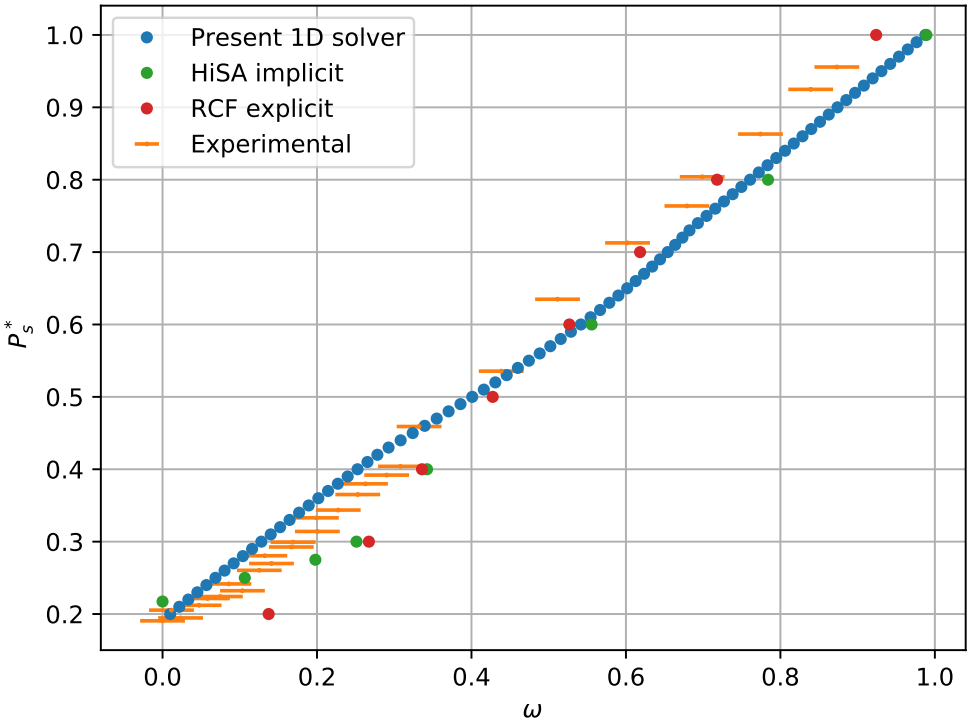

FIGURE 22: Linear calculation

6 Conclusions

The present thesis shows the development for a one dimensional model solver for a supersonic ejector. The model is capable of predicting the performance of an ejector with a given geometry and isentropic coefficients that take account for the mixing and frictional losses.

To achieve the objective, much research has been done, as it is explained in the report. The report has explanations for the working principle of ejectors, and all the set of equations used in the model are shown and explained. The model procedure is also explained and a copy of it is added in the Appendix.

The validation of the model shows that it is capable of predicting the ejector performance for a determined geometry (which is not shown for confidentiality reasons) with a good accuracy, and it also computes the vacuum level that it is predicted to arrive to.

The results show the accuracy of the present one dimensional model compared to CFD models (implicit HiSA and explicit RCF), and it is shown that performance levels are very similar to those achieved by HiSA solver, except for low-middle range of secondary pressure levels, where the difference increases.

The main objective was to develop a one dimensional model capable to be used among a CFD model to be able to achieve a geometry optimization of an ejector. The results show that the present one dimensional model is able of predicting the minimum pressure levels achieved for a given ejector with considerable high accuracy.

The developed one dimensional (1D) solver computes a maximum vacuum level of 80% (minimum $P_s^* = 0.2$) for the ejector with the geometry of [1], while experimental results show a vacuum level of 81% (minimum $P_s^* = 0.19$). The minimum entrainment ratio obtained by the model is $\omega = 0.0099$ with the minimum secondary pressure, in front of the $\omega = 0.0116 \pm 0.029$ obtained in experimental results.

7 Budget

The budget presents the different tasks that have been done in order to develop the engineering project, the necessary hours to develop the tasks and the total price needed to elaborated the different activities.

This project consists in the development of an open one dimensional solver made with Python. Therefore, the price of the project consists only in the salary that would be paid to a junior engineer.

The average salary for a junior engineer in Spain [26] is 26,309 € per year. The working days are approximately 273 days per year, with 8 working hours per day, which yields to:

$$\text{Price/h} = \frac{26,309}{273 \times 8} \approx 12\,€/\text{h}$$

Once the price per hour is determined, it is necessary to calculate the working hours. The following table accounts for the different tasks and the hours.

TABLE 4: Hours required to complete each task

Task code	Task identification	Hours
1	Research & documentation	135 h
2	Documentation writing	80 h
3	Software development	165 h
Total		380 h

The Research & documentation accounts for the hours needed for the search of different studies and books needed to develop the project, as long as the hours needed to read and analyze all the necessary information. The documentation writing is the time needed to write the present report. Finally, the software development covers the different tasks performed to achieve the code implementation, as the tasks used for the presentation of the results. Fig. 23 includes the different tasks done for the software development, alongside the frame time that has been required.

Finally, once the total hours are known, the total cost can be calculated:

$$\text{Total Cost} = 380\,\text{h} \cdot 12\,€/\text{h} = 4,560\,€$$

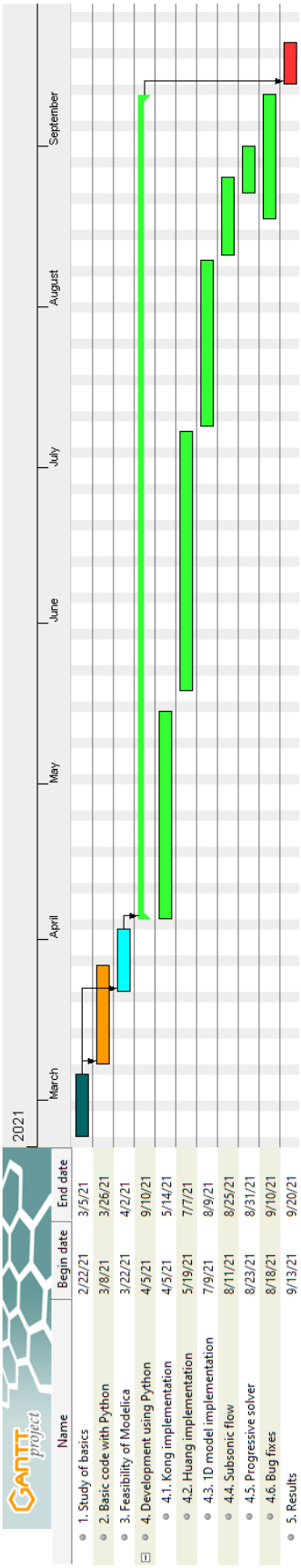

FIGURE 23: Project Gantt Chart

References

1. MACIA, Ll; CASTILLA, R.; GAMEZ-MONTERO, P. J.; CAMACHO, S.; CODINA, E. Numerical Simulation of a Supersonic Ejector for Vacuum Generation with Explicit and Implicit Solver in Openfoam. *Energies*. 2019-09-17, vol. 12, no. 18, p. 3553. ISSN 1996-1073. Available from DOI: 10.3390/en12183553.

2. KONG, F. S.; JIN, Y. Z.; KIM, H. D. Analytical and computational studies on the vacuum performance of a chevron ejector. *Shock Waves*. 2016-11, vol. 26, no. 6, pp. 771–788. ISSN 0938-1287, ISSN 1432-2153. Available from DOI: 10.1007/s00193-015-0618-8.

3. GRAZZINI, Giuseppe; MILAZZO, Adriano; MAZZELLI, Federico. *Ejectors for Efficient Refrigeration*. Cham: Springer International Publishing, 2018. ISBN 978-3319752433. Available from DOI: 10.1007/978-3-319-75244-0.

4. KRANAKIS, Eda Fowlks. The French Connection: Giffard's Injector and the Nature of Heat. *Technology and Culture*. 1982, vol. 23, no. 1, pp. 3–38. ISSN 0040165X, ISSN 10973729. Available also from: http://www.jstor.org/stable/3104441.

5. KNEASS, S.L. *Practice and theory of the injector*. John Wiley and Sons, 1898. ISBN 978-0554943671. Available also from: https://books.google.es/books/about/Practice_and_Theory_of_the_Injector.html?id=qUFMAAAAMAAJ&redir_esc=y.

6. *Brake (Vol. 4)*. Encyclopædia Britannica, 1911.

7. LEBLANC, Maurice. *Steam ejector apparatus*. US Patent No. 1461447, 1923-07. Available also from: https://patents.google.com/patent/US1461447.

8. GARCÍA DEL VALLE, Javier. *Eyectores para aplicaciones frigoríficas*. 2014. Available from DOI: 10.35376/10324/4901. PhD thesis. Universidad de Valladolid. Escuela de Ingenierías Industriales.

9. CHUNNANOND, Kanjanapon; APHORNRATANA, Satha. Ejectors: applications in refrigeration technology. *Renewable and Sustainable Energy Reviews*. 2004-04, vol. 8, no. 2, pp. 129–155. ISSN 13640321. Available from DOI: 10.1016/j.rser.2003.10.001.

10. SUN, Da-Wen; EAMES, Ian W. Performance characteristics of HCFC-123 ejector refrigeration cycles. *International Journal of Energy Research*. 1996, vol. 20, no. 10, pp. 871–885. Available from DOI: https://doi.org/10.1002/(SICI)1099-114X(199610)20:10<871::AID-ER201>3.0.CO;2-4.

11. SUN, Da-Wen; EAMES, I. W. Recent developments in the design theories and applications of ejectors - a review. *Journal of the Institute of Energy*. 1995, vol. 68, no. 475, pp. 65–79. Available also from: www.scopus.com.

12. HUANG, B.J.; CHANG, J.M.; WANG, C.P.; PETRENKO, V.A. A 1-D analysis of ejector performance. *International Journal of Refrigeration*. 1999-08, vol. 22, no. 5, pp. 354–364. ISSN 01407007. Available from DOI: 10.1016/S0140-7007(99)00004-3.

13. CHEN, WeiXiong; LIU, Ming; CHONG, DaoTong; YAN, JunJie; LITTLE, Adrienne Blair; BARTOSIEWICZ, Yann. A 1D model to predict ejector performance at critical and sub-critical operational regimes. *International Journal of Refrigeration*. 2013-09, vol. 36, no. 6, pp. 1750–1761. ISSN 01407007. Available from DOI: 10.1016/j.ijrefrig.2013.04.009.

14. KUMAR, Vikas; SACHDEVA, Gulshan. 1-D model for finding geometry of a single phase ejector. *Energy*. 2018-12, vol. 165, pp. 75–92. ISSN 03605442. Available from DOI: 10.1016/j.energy.2018.09.071.

15. HEMIDI, Amel; HENRY, François; LECLAIRE, Sébastien; SEYNHAEVE, Jean-Marie; BARTOSIEWICZ, Yann. CFD analysis of a supersonic air ejector. Part I: Experimental validation of single-phase and two-phase operation. *Applied Thermal Engineering*. 2009-06, vol. 29, no. 8, pp. 1523–1531. ISSN 13594311. Available from DOI: 10.1016/j.applthermaleng.2008.07.003.

16. VIRTO ALBERT, Luis. *Dinámica de gases*. 2017. ISBN 978-84-9880-692-2. Available also from: http://hdl.handle.net/2117/114130. OCLC: 1120450362.

17. FABRI, J.; SIESTRUNCK, R. Supersonic Air Ejectors. In: DRYDEN, H.L.; VON KÁRMÁN, Th. (eds.). Elsevier, 1958, vol. 5, pp. 1–34. Advances in Applied Mechanics. ISSN 0065-2156. Available from DOI: https://doi.org/10.1016/S0065-2156(08)70016-4.

18. MUNDAY, John T.; BAGSTER, David F. A New Ejector Theory Applied to Steam Jet Refrigeration. *Industrial & Engineering Chemistry Process Design and Development*. 1977, vol. 16, no. 4, pp. 442–449. Available from DOI: 10.1021/i260064a003.

19. JR, John D Anderson. *Modern Compressible Flow: With Historical Perspective*. 3rd ed. McGraw-Hill Series in Aeronautical and Aerospace Engineering, 2003. ISBN 0072424435.

20. *Normal shock wave equations*. NASA, [n.d.]. Available also from: https://www.grc.nasa.gov/www/k-12/airplane/normal.html.

21. SEITZMAN, Jerry M. *Fanno Flow - Thermodynamics*. Georgia Tech- College of Engineering - School of Aerospace Engineering, 2002-11. Available also from: http://seitzman.gatech.edu/classes/ae3450/fannoflow_two.pdf.

22. CHANSON, Hubert. 7 - Turbulent dispersion and mixing: 1. Vertical and transverse mixing. In: CHANSON, Hubert (ed.). *Environmental Hydraulics of Open Channel Flows*. Oxford: Butterworth-Heinemann, 2004, pp. 81–98. ISBN 978-0-7506-6165-2. Available from DOI: https://doi.org/10.1016/B978-075066165-2.50039-4.

23. WINTERTON, R.H.S. CHAPTER 6 - Fluid Flow. In: WINTERTON, R.H.S. (ed.). *Thermal Design of Nuclear Reactors*. Pergamon, 1981, pp. 84–105. ISBN 978-0-08-024215-6. Available from DOI: https://doi.org/10.1016/B978-0-08-024215-6.50010-3.

24. C.F., Colebrook; C.M., White. Experiments with fluid friction in roughened pipes. *Proc. R. Soc. Lond.* 1937, pp. 367–381. Available from DOI: http://doi.org/10.1098/rspa.1937.0150.

25. KIRKLAND, William M. A Polytropic Approximation of Compressible Flow in Pipes With Friction. *Journal of Fluids Engineering*. 2019-12-01, vol. 141, no. 12, p. 121404. ISSN 0098-2202, ISSN 1528-901X. Available from DOI: 10.1115/1.4043717.

26. GLASSDOR. *Junior Engineer in Madrid* [online]. 2021 [visited on 2021-09]. Available from: https://www.glassdoor.es/Sueldos/madrid-junior-engineer-sueldo-SRCH_IL.0,6_IM1030_KO7,22.htm.

A Python code

```
#Alex Martinez de Francisco 2021

#%%

#Implement different libraries
import math
import csv
import numpy as np
from scipy.optimize import fsolve
import time

#%%
#The solver function returns the entrainment ratio w, the back pressure Pc, the pressure of the secondary flow at section y-y and the mass flow rates of primary and secondary flows.
#The function takes as arguments the entrainment pressure. Other arguments are passed in to make the progressive iterations. It distinguishes between the first iteration (supersonic mode of operation) and the other iterations (subsonic mode).

def solver(first_solve, args):

    [Psy_prev, delta_vec, pc_vec, w_vec, Pc_crit, Ps_data] = args
    if first_solve:
        del pc_vec
    delta = delta_vec[-1]

    #Fluid parameters (constants, air)
    gamma = 1.4
    R = 287
    cp = 1004.5
    mu = 1.7894e-5

    #Primary and entrained flows pressures and temperatures
    Pp = 7.0e5
    Tp = 273+20
    Ps = Ps_data
    Ts = 273+20

    #Ejector geometry
    def area(d):
        A = np.pi * (d ** 2) / 4
        return A

    #Ejector geometries are not shown
    At = area()
```

```
    Ap1 = area()
    d2 =
    A2 = area(d2)
    Lm =

    #Ejector coefficients are not shown (commented reference values
     ↪  of Huang et al.)
    eta_p = #0.95
    eta_s = #0.85
    eta_py = #0.88
    psi_m = #0.80-0.82-0.84

    #Relations
    def computedot_mp(Pp, Tp, At):
        dotm_1 = Pp * At * np.sqrt(eta_p * gamma/R/Tp *
         ↪  (2/(gamma+1)) ** ((gamma+1)/(gamma-1)))
        return dotm_1

    def computeMp1(Mp1, args):
        [Ap1, At] = args
        eq = (Ap1 / At)**2 - 1 / (Mp1**2) * (2/(gamma+1) * ( 1 +
         ↪  (gamma-1) / 2 * (Mp1**2))) ** ((gamma+1)/(gamma-1))
        return eq

    def computeP(P0, M):
        P = P0/(1 + (gamma-1)/2 * (M ** 2)) ** (gamma/(gamma-1))
        return P

    def computeMpy(Mpy, args):
        [Pp1, Ppy, Mp1] = args
        eq = Ppy / Pp1 - (1 + (gamma-1)/2 * (Mp1 ** 2)) **
         ↪  (gamma/(gamma-1)) / (1 + (gamma-1)/2 * (Mpy ** 2)) **
         ↪  (gamma/(gamma-1))
        return eq

    def computeApy(Ap1, Mp1, Mpy):
        Apy = Ap1 * eta_py * Mp1 / Mpy * ((2 + (gamma-1) *
         ↪  (Mpy**2))/(2 + (gamma - 1) * Mp1 ** 2)) **
         ↪  ((gamma+1)/2/(gamma-1))
        return Apy

    def computedot_ms(Ps, Ts, Asy):
        dotm_1 = Ps * Asy * np.sqrt(eta_s * gamma/R/Ts *
         ↪  (2/(gamma+1)) ** (((gamma+1))/(gamma-1)))
        return dotm_1

    def computeTsy(Ts, Ps, Psy):
        Tsy = Ts * (Psy/Ps) ** ((gamma-1)/gamma)
        return Tsy
```

```
83
84      def computeve_sy(Psy, Tsy):
85          ve_sy = R * Tsy / Psy
86          return ve_sy
87
88      def computeVsy(Ts, Tsy):
89          Vsy = np.sqrt(2 * cp * (Ts-Tsy))
90          return Vsy
91
92      def computeTpy(Tp, Mpy):
93          Tpy = Tp * (1 + (gamma-1)/2 * Mpy**2) ** (-1)
94          return Tpy
95
96      def computeVpy(Tpy, Mpy):
97          Vpy = Mpy * np.sqrt(gamma * R * Tpy)
98          return Vpy
99
100     #Section m-m
101     def computeVm(dot_mp, dot_ms, Vpy, Vsy):
102         Vm = psi_m * (dot_mp * Vpy + dot_ms * Vsy) / (dot_mp +
            ↪  dot_ms)
103         return Vm
104
105     def computeTm(dot_mp, dot_ms, Vpy, Vsy, Tpy, Tsy):
106         Tm = ((dot_mp * (cp * Tpy + Vpy**2/2) + dot_ms * (cp * Tsy
            ↪  + Vsy**2/2))/(dot_mp+dot_ms) - Vm**2/2)/cp
107         return Tm
108
109     def computeMm(Vm, Tm):
110         Mm = Vm / np.sqrt(gamma * R * Tm)
111         return Mm
112
113     #Section 2-2
114     def computeP2(Pm, Mm):
115         P2 = Pm * (1 + 2 * gamma/(gamma+1) * (Mm**2-1))
116         return P2
117
118     def computeM2_sq(Mm):
119         M2_sq = (1 + (gamma-1)/2 * Mm**2) / (gamma * Mm**2 -
            ↪  (gamma-1)/2)
120         return M2_sq
121
122     #Section 2-2 to 3-3
123     def computeT2(Mm, Tm):
124         T2 = Tm * (((2 * gamma * Mm ** 2) - (gamma - 1)) * ((gamma
            ↪  - 1) * Mm ** 2 + 2)) / ((gamma + 1) ** 2 * Mm ** 2)
125         return T2
126
127     def computeRe(rho_2, V2, dh):
```

```
128         Re = rho_2 * V2 * dh / mu
129         return Re
130
131     def computef(f, Re):
132         d = np.log(10) * Re / 5.02
133         q = np.log(d) ** (np.log(d) / (np.log(d) + 1))
134         g = np.log(d / q)
135         z = np.log(q / g)
136         eq = 1 / np.sqrt(f) - 2 / np.log(10) * (np.log(d/q) + z * g
            ↪  / (g+1) * (1 + 3 * z / (6 * (g+1) ** 2 + 2 * z * (2 * g
            ↪  - 1))))
137         return eq
138
139     def computeK(M_sq):
140         K = (1 - M_sq)/(gamma * M_sq) + (gamma+1)/(2*gamma) *
            ↪  np.log(((gamma+1) * M_sq)/(2+(gamma-1)*M_sq))
141         return K
142
143     def solveM_sq(M_sq, args):
144         K = args
145         eq = K - (1 - M_sq)/(gamma * M_sq) - (gamma+1)/(2*gamma) *
            ↪  np.log(((gamma+1) * M_sq)/(2+(gamma-1)*M_sq))
146         return eq
147
148     def computeP3(P2, M2_sq, M3_sq):
149         P3 = P2 * np.sqrt(M2_sq / M3_sq) * ((1 + (gamma - 1) / 2 *
            ↪  M2_sq)/(1 + (gamma - 1) / 2 * M3_sq)) ** (1/2)
150         return P3
151
152     #Flow throw diffuser
153     def computePc(P2, M2_sq):
154         Pc = P2 * (1 + (gamma-1)/2 * M2_sq) ** (gamma/(gamma-1))
155         return Pc
156
157
158     #Solver
159
160     dot_mp = computedot_mp(Pp,Tp,At)
161     Mp1 = abs(fsolve(computeMp1, np.array([3,5]), args=[Ap1,
        ↪  At])[0])
162     Pp1 = computeP(Pp, Mp1)
163
164     # Different solutions for different modes of operation. Method
        ↪  of convergence
165     if first_solve:
166         Msy = 1
167         Psy = computeP(Ps, Msy)
168     else:
169         sum_Psy = 1.0e3
```

```
170             conver_error = False
171             if len(delta_vec)>2:
172                 if delta_vec[2]>delta_vec[1]:
173                     sum_Psy = 5.0e2
174                     if len(delta_vec)==3:
175                         print('Solving convergence error...')
176                         Psy = Psy_prev - 1.0e3
177                         conver_error = True
178                         print('Solved')
179 
180             if not conver_error:
181                 Psy = Psy_prev + sum_Psy * delta
182 
183         Ppy = Psy
184 
185         Mpy = fsolve(computeMpy, np.array([1,5]), args=[Pp1, Ppy,
            ↪  Mp1])[0]
186         Apy = computeApy(Ap1, Mp1, Mpy)
187         Asy = A2 - Apy
188 
189         if first_solve:
190             dot_ms = computedot_ms(Ps, Ts, Asy)
191 
192         # Section y-y
193         Tsy = computeTsy(Ts, Ps, Psy)
194         ve_sy = computeve_sy(Psy, Tsy)
195         Vsy = computeVsy(Ts, Tsy)
196         if not first_solve:
197             dot_ms = Vsy * Asy / ve_sy * np.sqrt(eta_s)
198 
199         Tpy = computeTpy(Tp, Mpy)
200         Vpy = computeVpy(Tpy, Mpy)
201 
202         #Section m-m
203         Vm = computeVm(dot_mp, dot_ms, Vpy, Vsy)
204         Tm = computeTm(dot_mp, dot_ms, Vpy, Vsy, Tpy, Tsy)
205         Mm = computeMm(Vm, Tm)
206         Pm = Psy
207 
208         #Section 2-2
209         P2 = computeP2(Pm, Mm)
210         M2_sq = computeM2_sq(Mm)
211 
212         #Section 2-2 to 3-3
213         dh = d2
214         T2 = computeT2(Mm, Tm)
215         rho_2 = P2 / (R * T2)
216         V2 = np.sqrt(M2_sq * gamma * R * T2)
217         Re = computeRe(rho_2, V2, dh)
```

```
218     f = fsolve(computef, np.array([0.0001]), args=Re)[0]
219     K = f*Lm/dh
220     K_M2 = computeK(M2_sq)
221     K_M3 = K_M2 - K
222     M3_sq = fsolve(solveM_sq, np.array([0.0001]), args=K_M3)[0]
223     K_new_M3  = computeK(M3_sq)
224 
225     if not round(K_M3,3) == round(K_new_M3,3):
226         M3_sq = 1
227 
228     P3 = computeP3(P2, M2_sq, M3_sq)
229 
230     #Flow through Diffuser
231     Pc = computePc(P3, M3_sq) #P3 and M3
232 
233 
234     if not first_solve:
235         pc_vec.append(Pc)
236         Pc_vector = pc_vec
237     else:
238         Pc_vector = [Pc]
239 
240     #Results
241     w = dot_ms/dot_mp
242     if not first_solve:
243         w_vec.append(w)
244         w_vector = w_vec
245     else:
246         w_vector = [w]
247 
248     #Convergence
249     delta = np.abs((Pc-Pc_crit)/Pc_crit)
250     if not first_solve:
251         delta_vec.append(delta)
252         delta_vector = delta_vec
253     else:
254         delta_vector = [delta_vec]
255 
256     return Pc, w, Pc_vector, w_vector, delta_vector, Psy, dot_mp,
      ↪  dot_ms
257 
258 
259 # The function solver_routine is capable of solving the flow
    ↪  properties for different secondary pressures. The arguments are
    ↪  the secondary pressure and the back pressure.
260 
261 def solver_routine(Ps_data, Pc_crit):
262 
263     #Initialization
```

```
264     Psy_prev = 0
265     Psy_vec = []
266     delta_vec = [1]
267     pc_vec = [0]
268     w_vec = [0]
269 
270     #Solver
271     Variables = solver(True, args=[Psy_prev, delta_vec, pc_vec,
        ↪  w_vec, Pc_crit, Ps_data])
272 
273     #Results
274     Pc = Variables[0]
275     Psy_prev = Variables[5]
276     Psy_vec.append(Psy_prev)
277     pc_vec = Variables[2]
278     w_vec = Variables[3]
279 
280     #Loop
281     #Declaring variables for the loop. Declaring maximum N
        ↪  iterations.
282     i = 0
283     N = 2000
284     critic_mode = False
285 
286     if Pc > Pc_crit:
287         critic_mode = True
288         return critic_mode, i, Variables
289 
290     while delta_vec[i]>1.0e-5 and critic_mode == False:
291 
292         Variables_sub = solver(False, args=[Psy_prev, delta_vec,
            ↪  pc_vec, w_vec, Pc_crit, Ps_data])
293 
294         #Pc = Variables_sub[0]
295         Pc_vector = Variables_sub[2]
296         w_vector = Variables_sub[3]
297         delta_vector = Variables_sub[4]
298         Psy_prev = Variables_sub[5]
299 
300         Psy_vec.append(Psy_prev)
301         delta_vec = delta_vector
302         pc_vec = Pc_vector
303         w_vec = w_vector
304 
305         if i>N:
306             break
307 
308         i += 1
309 
```

```
310     return critic_mode, i, Variables_sub
311 
312 #----------SaveResults----------
313 #The saveResults function takes as arguments the results of the
    ↪  solver and prints to txt files the results.
314 
315 def saveResults(Ps, dot_ms, w, case):
316     if case == 0:
317         file = open('../RESULTS/solver_data.txt', 'w',
            ↪  encoding='ISO-8859-1')
318 
319         file.write('Ps\t\t')
320         file.write('dot_ms\t\t\t\t')
321         file.write('w\n')
322 
323         for j in range(0, len(Ps)):
324             file.write('%.2f\t' % (Ps[j]))
325             file.write('%.21f\t\t' % (dot_ms[j]))
326             file.write('%.10f\n' % (w[j]))
327 
328     else:
329         file = open('../RESULTS/w_comparison.txt', 'w',
            ↪  encoding='ISO-8859-1')
330 
331         file.write('Ps\t\t')
332         file.write('w\n')
333 
334         for j in range(0, len(Ps)):
335             file.write('%.2f\t' % (Ps[j]))
336             file.write('%.10f\n' % (w[j]))
337 
338     file.close()
339 
340 
341 #-------------Comparison with experimental data---------
342 #Comparision_routine computes the flow properties for the same
    ↪  secondary pressures used for the experimental data. It reads
    ↪  the experimental secondary pressure from an external csv file.
343 
344 def comparisondata_routine(Pc_critic):
345     Ps_exp = []
346     with open('./Results/experimental.csv', newline='') as csvfile:
347         reader = csv.reader(csvfile, quotechar='|')
348         i = 0
349         for row in reader:
350             if not i==0:
351                 Ps_exp.append(float(row[2])*1.0e5)
352             i += 1
353     # print('Experimental data collected')
```

```
354     #Obtaining data with same pressure of the present model
355     Ps_enter = Ps_exp
356     help_savedata = []
357     w_savedata = []
358     for j in range(0, len(Ps_enter)):
359         [critic_mode, i, Variables] = solver_routine(Ps_enter[j],
            ↪  Pc_critic)
360         w_savedata.append(Variables[1])
361         # if math.isnan(w_savedata[j]):
362         #     Ps_savedata = Ps_enter[0:j]
363         #     w_savedata = w_savedata[0:j]
364         #     break
365 
366     saveResults(Ps_enter, help_savedata, w_savedata, case=1)
367 
368 #-------Main----------
369 #Main function. It has three options. One is set to false and the
    ↪  other two are set to true by default.
370 #Print_result prints the results (flow properties) for the specific
    ↪  Pc_critic and Ps given.
371 #run_solver runs the solver and save the results to an external txt
    ↪  file for the different given Pc_critic (constant, as it is the
    ↪  external pressure), and for different values of the secondary
    ↪  flow pressure (Ps_enter).
372 #experimental_comparison runs the solver for the specific secondary
    ↪  flow pressure values used for experimental and prints the
    ↪  results to an external txt file.
373 
374 def main():
375 
376     start_time = time.time()
377     Pc_critic = 1.0e5
378 
379     Ps = 1.0e5
380     [critic_mode, i, Variables] = solver_routine(Ps, Pc_critic)
381 
382     #Results
383     Print_result = False
384     if critic_mode and Print_result:
385         print('Total iterations:', i+1)
386         print('Critical mode operation:',critic_mode)
387         print('-------------------')
388         print('Pc =',Variables[0])
389         print('w =', Variables[1])
390         print('mp_flow =',Variables[6])
391         print('ms_flow =',Variables[7])
392         print('Running_time =',round(time.time()-start_time,5),'s')
393         print('-------------------')
394 
```

```
395     elif Print_result:
396         print('Total iterations:', i+1)
397         print('Critical mode operation:',critic_mode)
398         print('------------------')
399         print('Pc =',Variables[0])
400         print('w =', Variables[1])
401         print('mp_flow =',Variables[6])
402         print('ms_flow =',Variables[7])
403         print('delta =',Variables[4][-1])
404         print('Running_time =',round(time.time()-start_time,5),'s')
405         print('------------------')
406 
407 
408     # Progressively reduce Ps
409     Ps_enter = np.linspace(1.0e5, 0.0, 101)
410     dot_ms_savedata = []
411     w_savedata = []
412 
413     run_solver = True
414     if run_solver:
415         for j in range(0,len(Ps_enter)):
416             [critic_mode, i, Variables] =
                ↪  solver_routine(Ps_enter[j], Pc_critic)
417             dot_ms_savedata.append(Variables[7])
418             w_savedata.append(Variables[1])
419             if math.isnan(dot_ms_savedata[j]):
420                 Ps_enter = Ps_enter[0:j]
421                 dot_ms_savedata = dot_ms_savedata[0:j]
422                 w_savedata = w_savedata[0:j]
423                 break
424 
425         saveResults(Ps_enter, dot_ms_savedata, w_savedata, case=0)
426 
427 
428     experimental_comparison = True
429     if experimental_comparison:
430         comparisondata_routine(Pc_critic)
431 
432 
433     print('----------------------')
434     print('Running_time =',round(time.time()-start_time,5),'s')
435 
436 if __name__ == "__main__":
437     main()
```